



저작자표시-비영리-변경금지 2.0 대한민국

이용자는 아래의 조건을 따르는 경우에 한하여 자유롭게

- 이 저작물을 복제, 배포, 전송, 전시, 공연 및 방송할 수 있습니다.

다음과 같은 조건을 따라야 합니다:



저작자표시. 귀하는 원저작자를 표시하여야 합니다.



비영리. 귀하는 이 저작물을 영리 목적으로 이용할 수 없습니다.



변경금지. 귀하는 이 저작물을 개작, 변형 또는 가공할 수 없습니다.

- 귀하는, 이 저작물의 재이용이나 배포의 경우, 이 저작물에 적용된 이용허락조건을 명확하게 나타내어야 합니다.
- 저작권자로부터 별도의 허가를 받으면 이러한 조건들은 적용되지 않습니다.

저작권법에 따른 이용자의 권리는 위의 내용에 의하여 영향을 받지 않습니다.

이것은 [이용허락규약\(Legal Code\)](#)을 이해하기 쉽게 요약한 것입니다.

[Disclaimer](#)

공학박사 학위논문

Development of Micro-Meter  
Thin-Film Solid Oxide Cells by  
Sputtering Process for Reversible  
Operation at Low Temperature  
(500 °C)

스퍼터링 공정을 이용한 저온(500 °C) 가역작동  
마이크로미터 박막 고체산화물전지의 개발

2022년 2월

서울대학교 대학원

기계항공공학부

이 상 훈

# Development of Micro-Meter Thin-Film Solid Oxide Cells by Sputtering Process for Reversible Operation at Low Temperature (500°C)

지도교수 차 석 원

이 논문을 공학박사 학위논문으로 제출함  
2021년 10월

서울대학교 대학원  
기계항공공학부  
이 상 훈

이상훈의 공학박사 학위논문을 인준함  
2021년 12월

위 원 장 안 성 훈 (인)

부위원장 차 석 원 (인)

위 원 이 윤 석 (인)

위 원 조 구 영 (인)

위 원 이 윤 호 (인)

# Abstract

There is a growing demand for green hydrogen as the global climate crisis is imminent, and related laws and regulations are passed yearly. However, the high production cost obstructs the spread out of the green hydrogen. Green hydrogen, produced by water electrolysis, consumes immersive energy in its production process. Therefore, it has been necessary to reduce thermal and electrical energy consumed by electrolysis cells. Thus, the cells should achieve high efficiency in order to operate at a lower temperature ( $<600^{\circ}\text{C}$ ) and efficiently produce hydrogen without parasitic loss.

Transforming SOEC into a thin-film platform can solve this issue by enabling smooth passage of reactants and products and vigorous reaction kinetics. Therefore, this thesis aims to develop thin film reversible solid oxide cells (RSOC) that operate at low temperatures ( $500^{\circ}\text{C}$ ). Magnetron sputtering process was mainly utilized to fabricate the thin film solid oxide cells (SOC). As a result of optimization on each component of the cells, alumina support, Ni-YSZ hydrogen electrode, YSZ electrolyte, LSCF-GDC oxygen electrode, the cell achieved a record-breaking current density value at  $500^{\circ}\text{C}$  and 1.3V, the thermoneutral voltage, and superior

reversibility, which has never been reported with thin film platforms.

Anodic aluminum oxide templates were used as a support for thin film RSOC. The average pore diameter of the templates was examined in terms of RSOC performance. Ni-YSZ cermet served as a steam electrode, and its composition, thickness, and microstructure were optimized for improved reversibility. YSZ electrolyte was optimized in the fabrication process by changing target-substrate distance and substrate rotation speed. The cell already achieved the record-breaking performance only by optimizing YSZ at 1.3V. It showed substantially improved polarization resistance primarily attributed to the enhanced electrolyte-oxygen electrode interfacial property. Finally, an oxygen electrode was developed using the co-sputtering method to fabricate thin film LSCF-GDC. Various compositions of LSCF-GDC were attempted, and the best-performing combination and thickness were derived. Columnar thin film LSCF-GDC electrode was first demonstrated by the co-sputtering method.

By optimizing each component, 1.15 A/cm<sup>2</sup> of electrolysis current at 1.3V and 500°C was achieved with 50:50 H<sub>2</sub>O and H<sub>2</sub> (50:50) mixture fuel gas. This current density is the highest electrolysis current density at the thermoneutral voltage and 500°C

among all reported values, as far as the author is aware. Poor electrolysis current and reversibility improved considerably by restructuring and optimizing the microstructure of each element. It enabled improved operation at lower temperatures due to enhanced reaction kinetics on both fuel and oxygen electrodes and better ionic conductivity of the electrolyte. The thin film platform adopted solid oxide cells has proved itself as a suitable option for reversible operation.

**Keyword :** Reversible Solid Oxide Cells, Thin-Film, Sputtering, Thin-Film Solid Oxide Cells, Solid Oxide Electrolyzer Cells

**Student Number :** 2016-20699

# Table of Contents

Abstract.....	i
Table of Contents.....	iv
List of Figures.....	vii
List of Tables .....	xi
<b>1. Introduction.....</b>	<b>1</b>
1.1.    Necessities of Green Hydrogen.....	1
1.2.    Fundamentals and Potential of Reversible Solid Oxide Cells .....	5
1.3.    Issues in Reversible Solid Oxide Cells.....	1 0
1.4.    Thin–Film Reversible Solid Oxide Cells.....	1 4
1.5.    Thesis Outlines.....	1 7
<b>2. Effect of AAO specifications on RSOC Performance..</b>	<b>2 0</b>
2.1.    Introduction.....	2 0
2.2.    Experimental details.....	2 2
2.3.    Results and Discussions.....	2 5
2.4.    Conclusion.....	3 0
<b>3. Development of Ni–YSZ Steam Electrode and Its Functional Layer .....</b>	<b>3 2</b>
3.1.    Introduction.....	3 2

3.2.	Experimental Details .....	3 5
3.3.	Results and Discussions.....	3 8
3.3.1.	Determination of Steam Electrode Materials.....	3 8
3.3.2.	Optimization of Ni–YSZ Steam Electrode.....	4 2
3.3.3.	Development of Continuous Sputtering Process for Ni– YSZ Cathode Functional Layer .....	4 8
3.4.	Conclusion.....	5 0
<b>4.</b>	<b>Optimization of YSZ Sputtering Process .....</b>	<b>5 2</b>
4.1.	Introduction.....	5 2
4.2.	Experimental Details .....	5 4
4.3.	Results and Discussions.....	5 6
4.4.	Conclusion.....	6 1
<b>5.</b>	<b>Development of LSCF–GDC Oxygen Electrode for Oxygen Evolution Reaction .....</b>	<b>6 3</b>
5.1.	Introduction.....	6 3
5.2.	Experimental Details .....	6 5
5.3.	Results and Discussions.....	6 7
5.3.1.	Determination of optimum composition on electrolyte– supported cells .....	6 7
5.3.2.	Determination of optimum composition on AAO–based cells.....	7 0
5.3.3.	Investigation on Optimum Thickness of LSCF–GDC anode.....	7 2
5.4.	Conclusion.....	7 3

6. Concluding Remarks.....	7 5
Bibliography .....	7 8
국 문 초 록.....	8 5

# List of Figures

Figure 1-1. Projection of global greenhouse gas emissions and resulting global average temperature increase [2].....	1
Figure 1-2. Classification of hydrogen production process: Grey, blue, green hydrogen.....	2
Figure 1-3. Operating principles of RSOC: SOFC and SOEC [9] ....	6
Figure 1-4. Concept of RSOC operation coupled with renewable energy and hydrogen storage tank. ....	7
Figure 1-5. Principle of a solid oxide electrolysis cell (SOEC) for the co-electrolysis of steam/CO <sub>2</sub> , producing syngas and oxygen [10].....	8
Figure 1-6. Illustration of the central role and integration of the SOEC technology in a future energy system with the increased share of intermittent electricity from renewable sources such as wind and solar [11].....	9
Figure 1-7. Comparison of the microstructure of conventional SOEC and AAO-supported TF SOEC [32].....	16
Figure 2-1. Schematic illustrations of the microstructure of AAO templates and their surface and cross-sectional image [41].....	20
Figure 2-2. Surface image of AAO templates with the average pore diameter of 80 nm, 160 nm, and 250 nm, taken by FESEM. All images have the same scales. ....	22
Figure 2-3. Schematic illustrations of each type of cells. ....	24
Figure 2-4. Surface images and their binary phase formatted	

images of Ni-YSZ electrode deposited on AAO80 (a, d), AAO160 (b, e), AAO250 (c, f). All images are in same scale.....	2 6
Figure 2-5. Electrochemical characterization of cells deposited on different AAO templates. (a) Voltage sweep and (b) EIS Nyquist plot at 1.3 V .....	2 8
Figure 3-1. Schematic illustrations of cermet electrodes composed of nano-sized grains and micro-sized grains.....	3 2
Figure 3-2. Schematic illustrations and surface images of Ni-YSZ, Ni-GDC, and Pt steam electrode deposited on AAO80 templates. All images share the same scale bar. ....	3 9
Figure 3-3. Electrochemical tests done with different steam electrode materials. (a) Voltage sweep and (b) EIS spectra at 0.8V of cells with Ni-YSZ, Ni-GDC, and Pt steam electrode on AAO80. (c) Voltage sweep and (d) EIS spectra at 1.3V of cells with Ni-YSZ and Ni-GDC steam electrode on AAO160. ....	4 0
Figure 3-4. Schematic illustrations and surface image of NY25 and NY50 cells.....	4 3
Figure 3-5. Electrochemical test results of NY25 and NY50 cell on AAO250 templates.....	4 4
Figure 3-6. Surface FESEM image of NY25 electrode by thickness deposited on AAO250 substrate. (a) 800nm, (b) 1000nm, (c) 1200nm, (d) 1500nm. ....	4 5
Figure 3-7. Electrochemical tests for Ni-YSZ steam electrode by thickness. (a) Voltage sweep from 0.3V to 1.7V and (b)	

EIS Nyquist plot measured at 500°C and OCV.....	4 7
Figure 3-8. Surface FESEM image of (a) Ni-YSZ steam electrode and its functional layers (b-f). (b) N2Y1, (c) N2Y1.5, (d)N2Y2, (e)N1.5Y2, (f)N1Y2 .....	4 9
Figure 3-9. voltage sweep curve of cathodic functional layer applied cells measure at 500°C from 0.3V to 1.7V. ....	5 0
Figure 4-1. Ionic conductivity of selected solid oxide electrolyte materials as a reciprocal temperature function [63]. .	5 3
Figure 4-2. FESEM surface image of YSZ electrolyte deposited in various condition on Ni-YSZ steam electrode.....	5 6
Figure 4-3. 3D Topographic image of YSZ taken by AFM analysis. (a) 13L and (b) 13H. ....	5 7
Figure 4-4. XRD analysis of different YSZ films deposited on Si wafer.....	5 8
Figure 4-5. Electrochemical characterizations of TSD and SRS adjusted SOCs. (a) Voltage sweep from 0.3V to 1.7V, (b) EIS Nyquist plot at 500°C 1.3V.....	6 0
Figure 5-1. Surface and cross-sectional FESEM images of selected thin film LSCF-GDC combination deposited on Si wafer. .....	6 8
Figure 5-2. Voltage sweep of ScSZ electrolyte-supported cells with oxygen electrode of various LSCF-GDC composition measured at 500°C. Pt oxygen electrode was used as reference. ....	6 9
Figure 5-3. (a) Voltage sweep and (b) EIS Nyquist plot of LSCF- GDC anode adopted thin film RSOCs. ....	7 1

Figure 5-4. Voltage sweep from 0.3V to 1.7V on LSCF-GDC  
oxygen electrode cells with different thickness..... 7 3

Figure 6-1. Literature data on electrolysis current at 1.3V by  
different operating temperature..... 7 5

## List of Tables

Table 1-1. Comparison of PEMEC and SOEC .....	3
Table 2-1. Thickness of each component for the three types of cells .....	2 3
Table 3-1. Detailed process parameters of Ni-YSZ steam electrode composites.....	3 7
Table 3-2. XPS analysis result of NY25 and NY50 thin films.....	4 3
Table 4-1. Detailed experimental condition for each deposition cases. ...	5 5
Table 5-1. Detailed sputtering parameters for fabricating LSCF-GDC anode. .....	6 5

# 1. Introduction

## 1.1. Necessities of Green Hydrogen

With the passage of the Paris Climate Agreement in 2015, countries worldwide have reduced carbon emissions to meet the nationally determined contribution (NDC) goals. The Korean government has set its NDC goals in 2030 as a 40% decrease compared to greenhouse gas (GHG) emissions in 2018 to go along with the global trend [1].

Each country must take considerable actions to meet the targets. Developed countries, therefore, have planned their national energy blueprint to adopt a significant amount of renewable energy and convert it into a hydrogen economy.

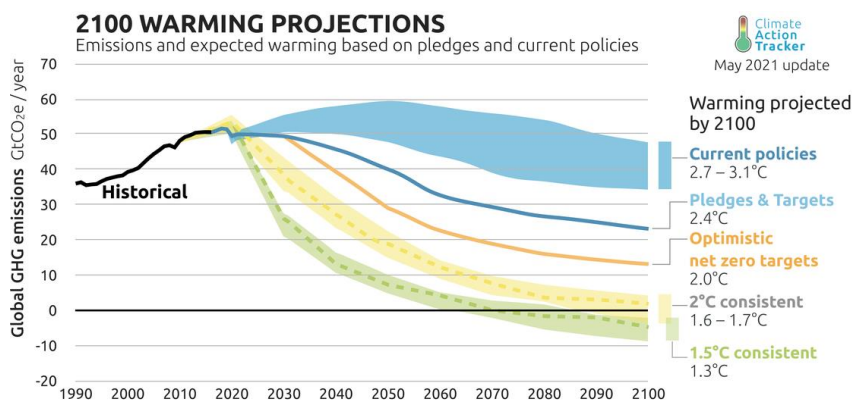


Figure 1–1. Projection of global greenhouse gas emissions and resulting global average temperature increase [2]

As fuel cells technology matures rapidly, their application fields have been broadened enormously. As a result, global hydrogen demand is expected to soar in the future. A report from Air Liquide projected that global hydrogen demand will surge 780% from 2020 to 2050 [3]. However, exploiting hydrogen as it used to is not suitable for achieving lower GHG emissions. Hydrogen is primarily produced by the steam methane reforming process using natural gas. As the process still uses fossil fuels, it emits carbons. Hydrogen production can be classified into three categories in terms of carbon emissions (Figure 1–2). One is grey hydrogen, produced by fossil fuels, as explained above. Another one is blue hydrogen. It is still made from fossil fuels, but CO<sub>2</sub> is captured and stored. As a result, the GHG emissions of this process fall a lot, but it still emits GHG, roughly 10~20% of the grey hydrogen process. The last one is green hydrogen, which is produced solely by water

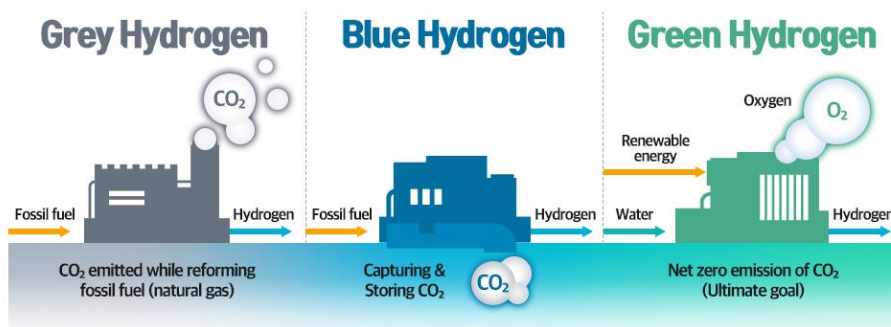
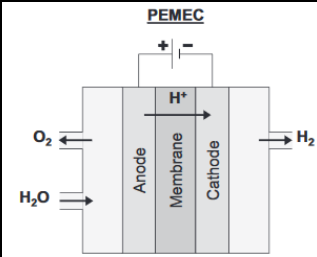
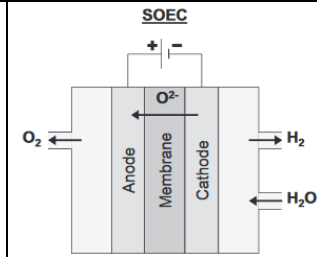


Figure 1–2. Classification of hydrogen production process: Grey, blue, green hydrogen

electrolysis and required electrical power is supplied by renewable energy. Thus, the carbon emission of the whole cycle of green hydrogen production is zero, including electricity generation and hydrogen production. Therefore, the hydrogen economy accompanied by green hydrogen production is the only way to significantly cut-off GHG emissions.

The electrolysis process is done by electrolyzer cells. There are a few kinds of electrolyzer cells, but two are commonly used: proton exchange membrane electrolyzer cells (PEMEC) and solid

Table 1–1. Comparison of PEMEC and SOEC

Classification	 <p style="text-align: center;">PEMEC</p>	 <p style="text-align: center;">SOEC</p>
	PEMEC	SOEC
Cathode/Anode Materials	Pt, Pt-Pd / RuO <sub>2</sub> , IrO <sub>2</sub>	Ni-YSZ / LSM-YSZ
Operating Temperature & Pressure	50-80 °C < 200 bar	600-1000 °C < 25 bar
Operational Cell Voltage	1.8 ~ 2.2V	0.7 ~ 1.5V
Conducting Ions	H <sup>+</sup>	O <sup>2-</sup>
H <sub>2</sub> Gas Purity	99.99%	99.9%

oxide electrolyzer cells (SOEC) (Table 1–1).

PEMEC uses a PFSA polymer membrane as an electrolyte, which conducts hydrogen ions, and the most common one is Nafion<sup>TM</sup> membranes. Unlike PEM fuel cells, PEMEC's anode, or oxygen electrode, comprises Ru– or Ir–based materials, while the cathode is composed of Pt or Pt–Pd. The membrane is sensitive to the purity of the feed water, so inlet water must be highly purified before reaching the cells. As hydrogen gas is solely produced in cathode without reactant flowing in, redundant post–processing is not required to collect hydrogen gas.

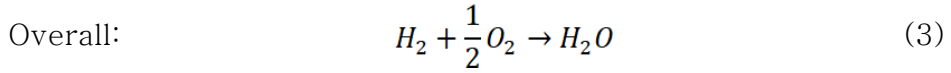
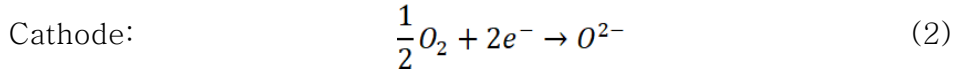
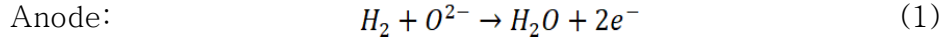
However, making PEM cells reversible is another complicated field of research. As mentioned earlier, the oxygen electrode materials must be separated due to their different catalytic activity towards oxygen reduction reaction and oxygen evolution reaction [4]. Furthermore, carbon contamination on the oxygen electrode can occur during oxygen evolution reactions from carbon–based gas diffusion layers due to the higher potential of the electrolysis process and higher humidity [5]. In addition, PEM cells require a gas diffusion layer (GDL) to have the opposite property: hydrophobicity in fuel cell mode to prevent flooding and hydrophilicity in electrolysis mode to supply water to the oxygen

electrode [6].

On the other hand, SOEC uses solid oxide materials as electrolytes. Yttria-stabilized zirconia (YSZ) is the most adopted electrolyte material. Since its optimum temperature range to conduct oxygen ions is over 600°C, its operating temperature typically falls between 600°C and 1000°C. Its high operating temperature allows SOECs to be highly efficient in many ways, i.e., catalytic reaction, reactant gas delivery, etc. [7]. Therefore, its required electrical energy is lower than PEMEC, which explains why SOEC operates at a lower voltage. Its components are the same as the SOFC's material, so there are no obstacles to reversible operation [8]. However, hydrogen is produced at the same side where steam is supplied, so a separator for separating steam from hydrogen gas is required in the SOEC system.

## **1.2. Fundamentals and Potential of Reversible Solid Oxide Cells**

As previously described, reversible solid oxide cells (RSOC) can operate as fuel cell (SOFC) mode and electrolyzer (SOEC) mode. In SOFC mode, half-reactions of each electrode and overall reaction are as follow:



Hydrogen oxidation reaction (HOR) takes place in the anode (fuel electrode), and oxygen reduction reaction (ORR) takes place in the cathode (oxygen electrode).

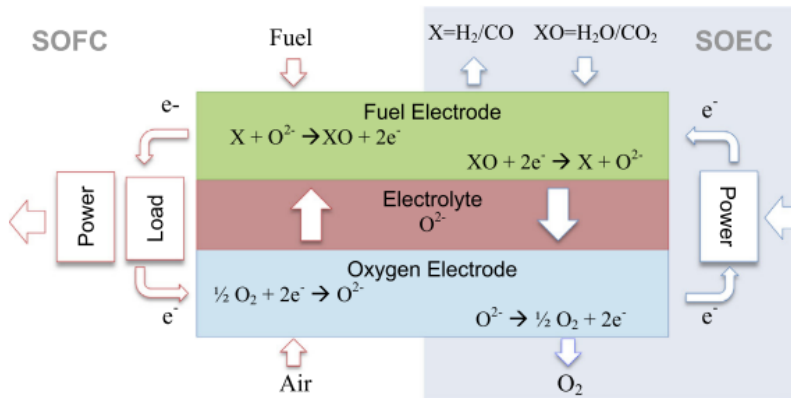
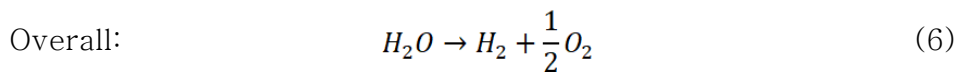
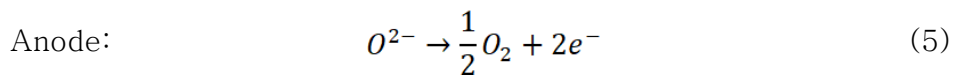
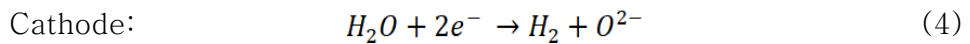


Figure 1–3. Operating principles of RSOC: SOFC and SOEC [9]

On the other hand, half–reactions of each electrode and overall reaction of SOEC are written as:



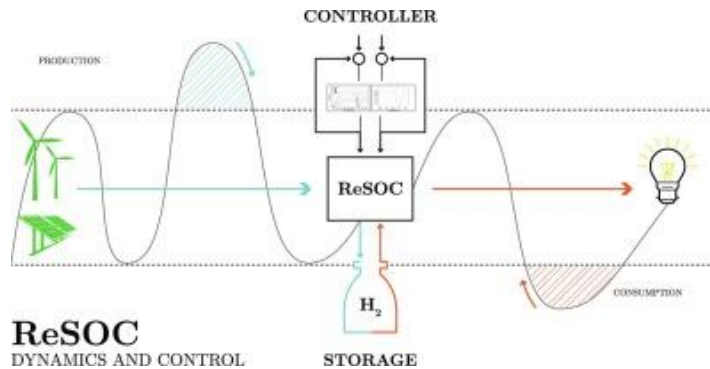


Figure 1–4. Concept of RSOC operation coupled with renewable energy and hydrogen storage tank.

Hydrogen evolution reaction (HER) occurs in the cathode (fuel electrode), and oxygen evolution reaction (OER) occurs in the anode (oxygen electrode) to complete the whole water–splitting reaction. It can be found that each electrode deals with the same reactants, although the reaction acts in reverse. The reversibility of RSOCs can play an essential role in the future energy roadmap. RSOC systems can produce green hydrogen and electricity with renewable energy and hydrogen storage facilities. Depending on the electricity price and the amount of available renewable energy, it can decide which to produce. When electricity price from the grid is low or surplus electrical power from renewable sources exists, RSOC can operate in SOEC mode to exploit electricity, producing hydrogen to store in the storage tank. On the other hand, when the electricity price is high, or electricity generated from renewable sources is insufficient, RSOC can operate in SOFC mode to generate

additional electricity by utilizing the stored hydrogen gas and selling it to the grid. This concept would significantly improve the primary drawback of renewable energy sources, its intermittency.

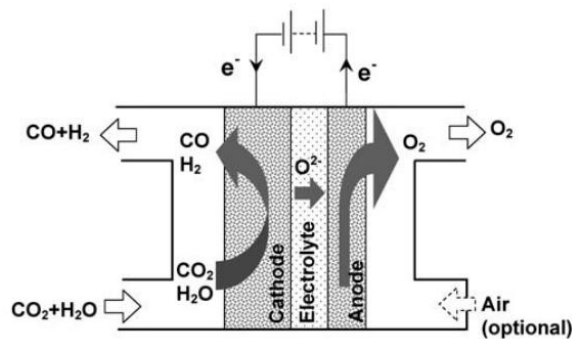
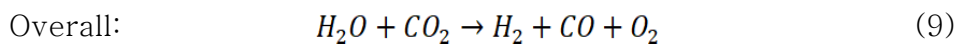
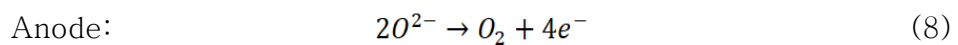
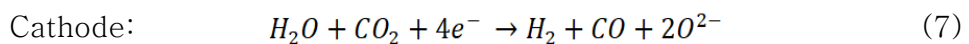


Figure 1–5. Principle of a solid oxide electrolysis cell (SOEC) for the co–electrolysis of steam/CO<sub>2</sub>, producing syngas and oxygen [10].

Another field where SOEC can take a role, other than just hydrogen production, is the production of synthetic fuels. Other than steam electrolysis, SOEC can produce syngas, a mixture of hydrogen and carbon monoxide, from the input of steam and carbon dioxide (Figure 1–5), which is called co–electrolysis. Reactions at each electrode and the overall reaction are written as follow:



Syngas is versatile gas that can synthesize fuels and various chemicals. Synthetic gasoline or diesel can be produced using syngas through Fischer–Tropsch (F–T) synthesis [12]. If the SOEC system is fed with captured  $\text{CO}_2$  to produce syngas via co–electrolysis, synthetic gasoline or diesel fuel can be synthesized while achieving net carbon–emission zero.

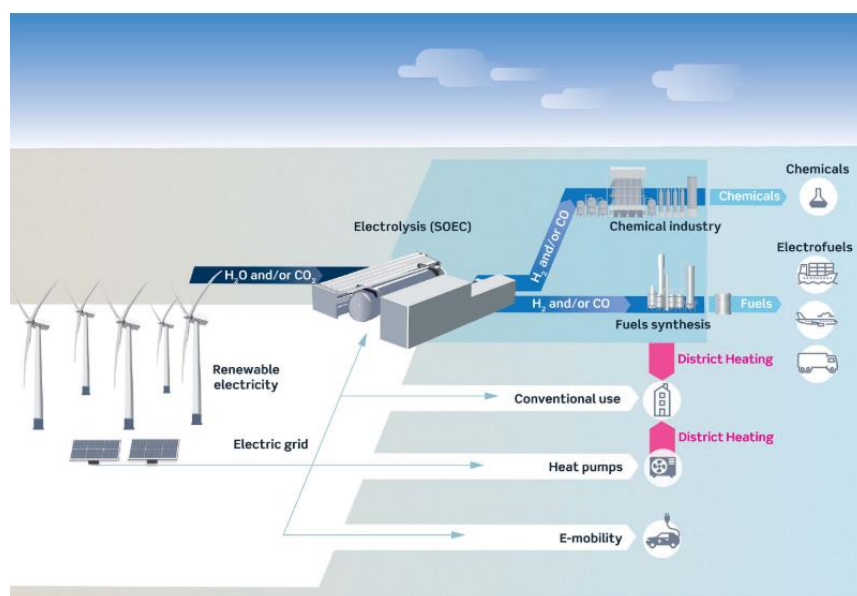


Figure 1–6. Illustration of the central role and integration of the SOEC technology in a future energy system with the increased share of intermittent electricity from renewable sources such as wind and solar [11].

The material generally employed for the electrolyte of SOECs is yttria–stabilized zirconia (YSZ), which has high ionic conductivity and strong chemical stability in both reducing and oxidating environments. The fuel electrode, or steam electrode, and the

oxygen electrode usually employs Ni-YSZ cermet and  $\text{La}_{1-x}\text{Sr}_x\text{MnO}_{3-\delta}$  (LSM) – or  $\text{La}_{1-x}\text{Sr}_x\text{Co}_y\text{Fe}_{1-y}\text{O}_{3-\delta}$  (LSCF) – based materials, respectively. These materials are generally employed in SOFCs as well. Although the same materials can activate in both reactions, there are several distinguished degradation phenomena in SOECs due to their higher applied voltage and more concentrated steam of the feed gas.

### 1.3. Issues in Reversible Solid Oxide Cells

As mentioned previously, several unique exacerbations occur when SOECs operate, which hardly occur in SOFC mode. Anode, or oxygen electrode, is the most vulnerable and rate-determining component in SOECs. It contributes a significant part to the whole degradation. Several degradation mechanisms are attributed to its high operating temperature, increased oxygen partial pressure, and the high anodic potential applied [13]. Since oxygen is produced in the anode through oxygen evolution reactions, it has high oxygen partial pressure ( $p_{O_2}$ ) at triple phase boundaries (TPB) where the reaction takes place. As the local distribution of the oxygen partial pressure is different from the reaction sites to the bulk flow channel, critical issues stem from this phenomenon.

Chen et al. investigated the delamination mechanism of LSM anode in SOEC [14]. Under low electrolysis current, excess oxygen is incorporated in the lattice of the LSM anode. It facilitates shrinkage of LSM lattice, resulting in local tensile stress around the lattice. It develops into micro-cracks, and consequently, delamination occurs due to excessive oxygen gas formed and resulting pressure in the cracks. Under the high current, the formation of a detrimental secondary phase,  $\text{La}_2\text{Zr}_2\text{O}_7$ , accompanies the delamination [15]. LSM/YSZ interface undergoes severe morphological changes, becoming more severe as the polarization resistance increases. According to the data from Chen,  $\text{La}_2\text{Zr}_2\text{O}_7$  formation is thermodynamically favorable ( $\Delta G < 0$ ) when  $p_{\text{O}_2}$  is more significant than 3.7 atm [16].

LSCF-based materials are another candidate commonly chosen as oxygen electrodes in SOEC. GDC barrier sits between LSCF and YSZ electrolyte to prohibit the formation of harmful secondary phases. However, despite the presence of the blocking layer, the LSCF electrode suffers from secondary phase formation, such as  $\text{SrZrO}_3$  or  $\text{Co}_3\text{O}_4$  [13]. From a set of long-term tests ( $> 1\text{kh}$ ) on Ni-YSZ|YSZ|GDC|LSCF-GDC cells done by Laurencin et al., the authors observed diffusion of Sr and Co from LSCF into GDC/YSZ interface [17]. Since Co is a B-site element in the LSCF perovskite

structure that dramatically improves the electrocatalytic ability, the hopped out Co leads to the loss of LSCF performance. LSCF-based SOEC also suffers from delamination. Pan et al. observed and revealed the mechanism of LSCF anode delamination after operation of SOEC for 24 hr at 800°C and 1 A/cm<sup>2</sup> anodic current [18]. The formation of the SrZrO<sub>3</sub> layer is pointed to as the cause for the delamination, which is induced by oxygen generation at the SrZrO<sub>3</sub>-YSZ interface. Wu et al. revealed that even conventional materials, LSC-YSZ, can significantly improve their OER performance by adopting linear and low-tortuosity structures on the oxygen electrode [19]. The advantages of MIECs, such as intrinsic conductivity and catalytic activity, are limited by traditional sponge-like high tortuosity electrode structures because of the sluggish oxygen generation and diffusion kinetics. By adopting the newly designed honeycomb-architecture LSC-YSZ, the cell showed no noticeable performance degradation at 2.0 A/cm<sup>2</sup> for 6 hr at 800°C. In comparison, the conventional LSC-YSZ underwent an abrupt voltage increase at 1.2 A/cm<sup>2</sup> at 800°C within 0.67 h.

Apart from SrZrO<sub>3</sub> layer formation due to Sr and Zr inter-diffusion of perovskite anode and YSZ electrolyte, several reports pointed out inter- or intra-granular pores formation within YSZ in SOEC operation. Knibbe et al. found the intergranular fracture and

pore formation along the grain boundaries of YSZ in the vicinity of the anode/electrolyte interface after SOEC operation at  $1-2 \text{ A/cm}^2$  [20]. Laguna-Bercero et al. investigated the correlation between electrolyte degradation and high cell voltage in cathode-supported microtubular YSZ-based SOEC at voltages up to 2.8V [21]. The study revealed that severe electrolyte reduction occurred in the operated cells, which formed voids at the grain boundaries of the dense YSZ electrolyte. Internal closed pores in YSZ electrolytes were critical to electrolyte degradation. Jiang et al. observed significant microstructure differences between the center and surroundings of the cavity caused by severe structural damage between LSM and YSZ [22]. The microstructure differences were come from the different microstructure of the initially closed pore and fractured YSZ surfaces, respectively.

Cathode, or steam electrode, is generally composed of Ni-YSZ cermet materials. These Ni-YSZ electrodes suffer from Ni depletion in the cathode/electrolyte interface and volatile  $\text{Ni(OH)}_2$  species formation in SOEC operation. High steam ratio and local steam concentration distribution cause the issues. The et al. observed Ni coarsening in the inner part of the electrode while Ni is depleted in the TPB region after 9000 h of SOEC operation at  $-1 \text{ A/cm}^2$  and  $780^\circ\text{C}$  [23]. It resulted in doubled electrolyte thickness,

Ni agglomeration in the inner part of the cathode, and TPB length decrease. Nickel in the electrode can react with water to form volatile species, such as  $\text{Ni(OH)}_2$ . These species diffuse and deposit on the electrolyte's surface, subsequently reduced to the metallic phase of Ni. When the temperature is below  $1000^\circ\text{C}$ , the critical steam content in hydrogen fuel gas for  $\text{Ni(OH)}_2$  to be stable with loss of Ni and NiO is 20% [24].

#### 1.4. Thin-Film Reversible Solid Oxide Cells

As surveyed in the previous section, most of the degradation phenomena stem from high operating temperature or poor gas transport due to closed pore and tortuous microstructure, etc. Gubner et al. investigated the mole fraction of the hydroxide  $\text{Ni(OH)}_2$  formed from the Ni-YSZ electrode in SOFC operation of 0.9V at  $950^\circ\text{C}$  with a fuel gas mixture of 34% of hydrogen 66% of steam [25]. The study calculated the mole fraction decreases from  $2 \cdot 10^{-9}$  at  $950^\circ\text{C}$  to  $5 \cdot 10^{-12}$  at  $700^\circ\text{C}$ . Including nickel-containing volatile species, many other detrimental phenomena are considerably subjected to operating temperature. Therefore, the lower operating temperature would significantly improve performance loss from those damaging behaviors. However,

overcoming lower ionic conductivity and loss of catalytic and electrochemical activity are other problems to confront.

The major causes of the issues in the anode or the anode/electrolyte interface are high oxygen partial pressure around the interface and TPB and its gradient from TPB to bulk flow channel. The study mentioned above by Wu et al. surmounted these issues by adopting honeycomb-architecture LSC-YSZ [19]. To conquer the oxygen partial pressure issue, securing straight pores and less tortuous electrode structure are the critical factors.

Combining these two strategies, letting the operating temperature lower and having the straight pores, thin-film solid oxide cells seem to be the suitable platform for realizing the requirements. In the SOFC field, significant progress has been made by adopting a thin-film platform over the past few years. Typically, there are two kinds of thin-film solid oxide fuel cells (TF-SOFC): free-standing and substrate-supported SOFCs [26, 27]. The free-standing type of SOFCs can accommodate electrolyte thickness down to tens of nanometers [28] so that this type can surpass any other platforms with superior initial performance [29]. However, its mechanical stability and physical robustness are yet to be solved. On the other hand, vibrant research has been done for years on the

other type, substrate-supported thin-film SOFCs. Several research groups achieved exceptional performance [29, 30], direct carbon-fueled operation, and over tens of hours of operation using the platform [31].

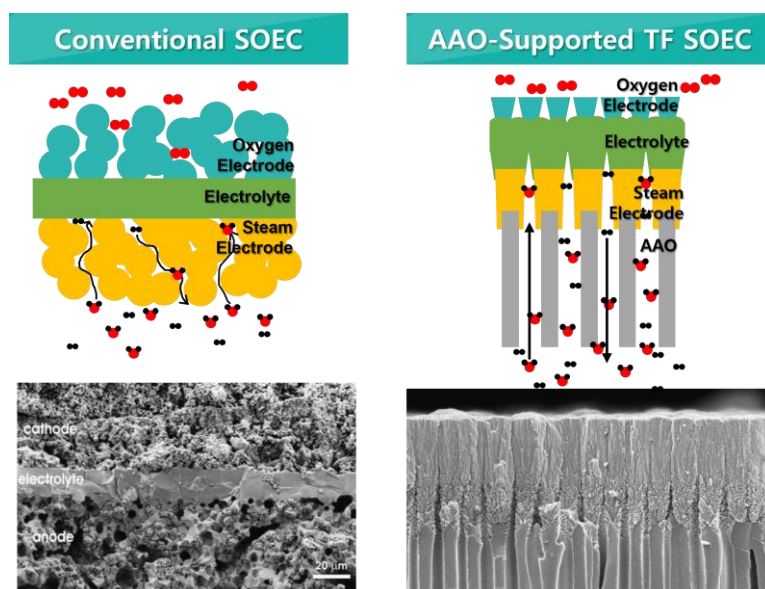


Figure 1-7. Comparison of the microstructure of conventional SOEC and AAO-supported TF SOEC [32].

Among the substrate-supported TF-SOFCs, anodic aluminum oxide (AAO)-supported cells have distinguished advantages to overcome the issues previously mentioned in the SOEC field. The inherent straight pores of the AAO templates enable solid oxide cells to have smooth mass transport to the reaction area. It will mitigate the steam concentration gradient from TPB to the inner part of the electrode.

In addition, using sputtering as TF SOC fabrication processes possess several advantages. Sputtering is one of the widely utilized physical vapor deposition (PVD) processes, which exhibit virtues of manipulative, straightforward, versatile, and efficient process time, etc. [33]. For fabricating SOFCs, using sputtering can build cermet electrodes, solid oxide electrolytes, or even perovskite electrodes without going through tens of hours of high-temperature sintering [34–40]. Furthermore, inherent columnar growth tendencies of sputter-deposited films function as suitable recipes to fabricate reactant-accessible electrodes.

## 1.5. Thesis Outlines

In this sense, this thesis aims to develop thin-film reversible solid oxide cells (TF RSOC) by the sputtering process for operating at low temperatures (500°C). All of the components of the TF RSOC were fabricated using the magnetron sputtering process. Each part is composed of conventional materials, which have been used in the field for a long. In this way, this study will verify that a significant leap in the electrochemical performance of RSOC can be made by adopting an appropriate fabrication process and platform, even with conventional materials. The steam electrode was made by the co-

sputtering process using Ni and YSZ. YSZ electrolyte was subsequently deposited on the steam electrode by radiofrequency (RF) magnetron sputtering. Finally, the LSCF–GDC oxygen electrode was deposited on the electrolyte layer using the co-sputtering method with LSCF oxide and Gd–Ce alloy targets. Each chapter will deal with how the components were optimized in process parameters and characterized via various analysis methods. The detailed summary of each chapter is described as follow:

- Chapter 2 deals with the effect of the physical specification of the AAO template on RSOC performance. Specifically, a pore size of AAO templates was differentiated into three cases. TF RSOCs with the same materials were fabricated, and their electrochemical performance was mainly discussed.
- Chapter 3 focuses on the Ni–YSZ steam electrode. This chapter is dedicated to determining the optimum combination of Ni and YSZ in the cermet and their microstructure to achieve an efficient hydrogen evolution reaction. Furthermore, a continuous deposition process developed here deposited an additional cathodic functional layer. The method fabricates cathode and cathode functional layer assembly at once. Correlations of the electrochemical performance and microstructure were examined. FESEM, FIB–SEM, EDS, XPS, AFM analyses were carried out.

- Chapter 4 seeks to find optimum YSZ deposition parameters to enhance the interface's ionic conductivity and charge transfer property. Geometrical parameters of the sputtering process were manipulated, such as target–substrate distance and rotation speed. Crystallinity and surface microstructure was analyzed via XRD, TEM, FESEM, and AFM. By optimizing the electrolyte, oxygen evolution reaction and reversibility of RSOC improved significantly.
- Chapter 5 investigates optimum chemical and physical specifications of the LSCF–GDC oxygen electrode. The co-sputtering method was utilized with the LSCF oxide and Gd–Ce alloy targets. XRD analysis was carried out to see whether perovskite phases were realized. The microstructure of LSCF–GDC was characterized and interpreted along with its impact on OER kinetics and reversibility of RSOC.
  - Chapter 6 encompasses all the achievements of the above in one cell and thoroughly investigates its electrochemical behavior in various conditions. The complete RSOC was electrochemically characterized according to different operating temperatures.

## 2. Effect of AAO specifications on RSOC Performance

### 2.1. Introduction

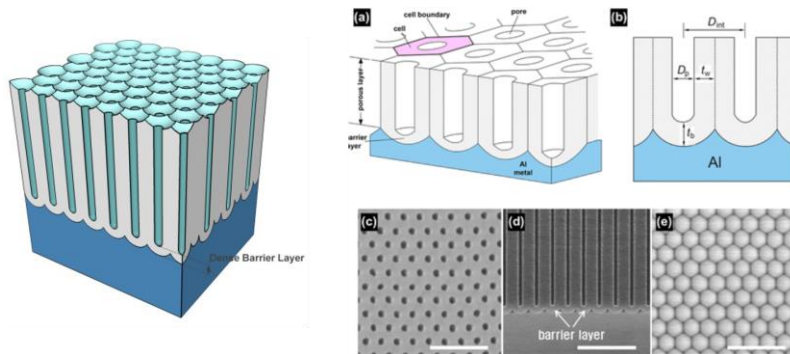


Figure 2-1. Schematic illustrations of the microstructure of AAO templates and their surface and cross-sectional image [41].

AAO is a self-organized material with honeycomb-like structures formed by high density uniformly distributed nanopores. AAO is manufactured through electrochemical oxidation, or anodization, of aluminum, balancing the growth and the localized dissolution of aluminum. The pores can be controlled with great precision of pore size from as low as a few nanometers to as high as hundreds of nanometers. The pores' length can range from a few tens of nanometers to a few hundred micrometers [41]. Modifications on the surface or cross-sectional shape of the pores can be made by adjusting the process parameters or introducing

additional processes, such as imprinting mold or pulsing the oxidation current.

For years, anodic aluminum oxide (AAO) templates have been used as a substrate for thin-film solid oxide fuel cells [26]. Due to its inherent pores, AAO-supported TF SOFC has its strength in establishing nanoporous columnar fuel electrodes. It helped the cells to achieve agile hydrogen oxidation reaction kinetics even in lower operating temperatures down to 500°C [30, 42–44].

Applying the AAO template to SOEC would bring more benefits. The et al. emphasized that a high steam ratio in the fuel gas and local steam concentration accelerate volatile species formation, such as Ni(OH)<sub>2</sub> [23]. Establishing straight and low-tortuosity pores can be a solution to alleviate localized steam concentration problems. Utilizing an AAO-supported platform can be an excellent option for realizing low-temperature operating RSOC.

This chapter aims to see the effects of specifications of the AAO template on the electrochemical performance of RSOC. Specifically, the pore diameter was set as the main parameter, and other parameters, such as template thickness or dimension, were selected as constant. Previously our research group researched the effect of AAO pore size and Ni anode thickness on SOFC [45, 46].

The study dealt with two different pore sizes of AAO Ni anode thickness was varied into three cases for each AAO type. By optimizing the pore size and the anode thickness, the maximum power density of the TF SOFC improved over 20% [45]. This chapter will further examine the correlation between AAO pore diameter and RSOC's performance. Unlike SOFC, SOEC bears critical issues regarding a steam concentration on the fuel electrode side, especially when coupled with Ni-based electrode. Although a thorough long-term operation to see Ni relocation was not performed, the effect of the higher steam concentration on hydrogen evolution reaction (HER) and RSOC performance was investigated.

## 2.2. Experimental details

Anodic aluminum oxide (AAO) templates (InRedox, U.S.A.)

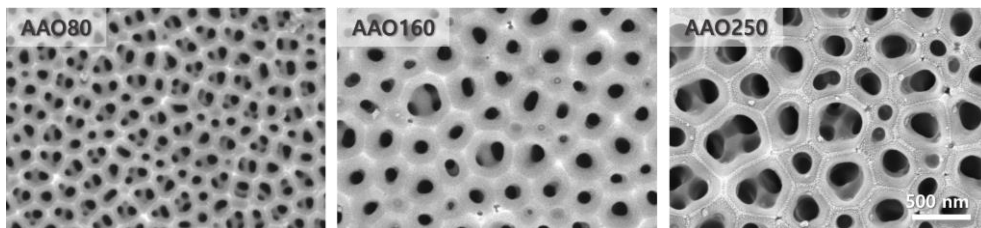


Figure 2–2. Surface image of AAO templates with the average pore diameter of 80 nm, 160 nm, and 250 nm, taken by FESEM. All images have the same scales.

have been used as a substrate. The dimension and the thickness of the AAO template were fixed as 1 cm by 1 cm and 100  $\mu\text{m}$ . The average pore size of the template was varied into three cases: 80nm (AAO80), 160nm (AAO160), and 250nm (AAO250). Ni-YSZ fuel electrode was deposited on the substrate by the co-sputtering method. Ni metal target (VTM, South Korea) and Y/Zr (16:84) alloy target (RND Korea, South Korea) were used. During the process, high purity argon gas was flowed into the chamber to maintain 60 mTorr of the sputtering chamber pressure. Nickel was sputtered using a DC power source with 200W power applied. At the same time, the Y/Zr alloy target was sputtered with 25W of RF power source applied. Target-substrate distance and rotation speed were fixed as 10 cm and 10.0 rpm, respectively.

Table 2-1. Thickness of each component for the three types of cells

Classification	AAO80	AAO160	AAO250
AAO Pore size	$80 \pm 10$ nm	$160 \pm 20$ nm	$250 \pm 30$ nm
AAO Porosity	$15 \pm 2\%$	$16 \pm 3\%$	$25 \pm 3\%$
Ni-YSZ Steam Electrode	450 nm	800 nm	800 nm
YSZ Electrolyte	1 $\mu\text{m}$		
Pt Oxygen Electrode	300 nm		

The thickness of the Ni-YSZ fuel electrode was differentiated

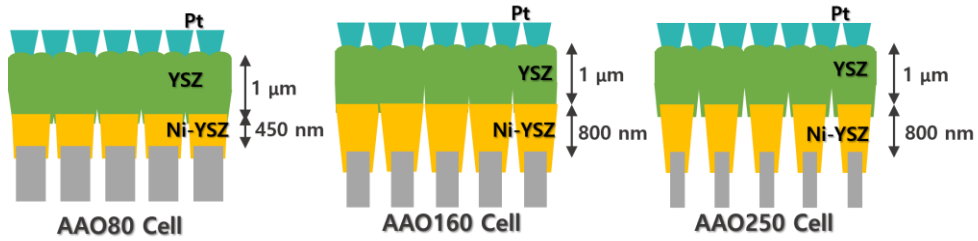


Figure 2–3. Schematic illustrations of each type of cells.

by each substrate. A larger pore of the substrates requires a higher height of the fuel electrodes to block the original pores of the substrate considering columnar growth tendencies of the sputter-deposited films. 450 nm of Ni–YSZ electrode was deposited on AAO80 substrate, while AAO160 and AAO250 substrates accommodated 800 nm of Ni–YSZ steam electrode.

All the cells have YSZ electrolyte and Pt oxygen electrodes deposited with identical parameters. The reactive sputtering process deposited YSZ solid oxide electrolyte on the steam electrode. During the procedure, Ar/O<sub>2</sub> (8:2) mixture gas was flowed into the chamber to maintain 10 mTorr, and 200W of RF power was applied to Y/Zr (16:84) alloy target. On top of the electrolyte, a platinum oxygen electrode was deposited with 100W of DC power used. A 60 mTorr of high purity argon gas filled the chamber during the sputtering process.

The cells completed as previously described went through

various analyses, including electrochemical characterization. I–V plot and electrochemical impedance spectroscopy (EIS) were carried out at 500°C operating temperature and 50 sccm of hydrogen gas flow with 50% steam content. To examine the reversible operation of the thin film solid oxide cells, the i–V plot was measured from 0.3V to 1.7V. EIS was estimated at 1.3 V to investigate SOC's electrochemical behavior at the electrolysis operation regime.

The microstructure of the completed cells was observed by field emission secondary electron spectroscopy (FESEM). Further verification of the results was confirmed through Multiphysics simulations using COMSOL Multiphysics.

### 2.3. Results and Discussions

Figure 2–4 shows the surface image of the deposited Ni–YSZ steam electrode on each AAO template. As thickness grows, grain size becomes larger, comparing 450 nm of Ni–YSZ on AA080 (figure 2–4. (a)) and 800 nm of Ni–YSZ on AA0160 and AA0250 (figure 2–4. (b) and (c)). To investigate the effect of the average pore size of AAO templates on the porosity of steam electrodes, the FESEM surface image was transformed into a binary phase, and

porosity was calculated accordingly. The image formatting and porosity analysis were performed using an image processing program called ImageJ, developed at the National Institutes of Health. The electrode's porosity on AAO80, AAO160, and AAO250 was calculated as 4.8%, 5.6%, and 10.0%, respectively. Although

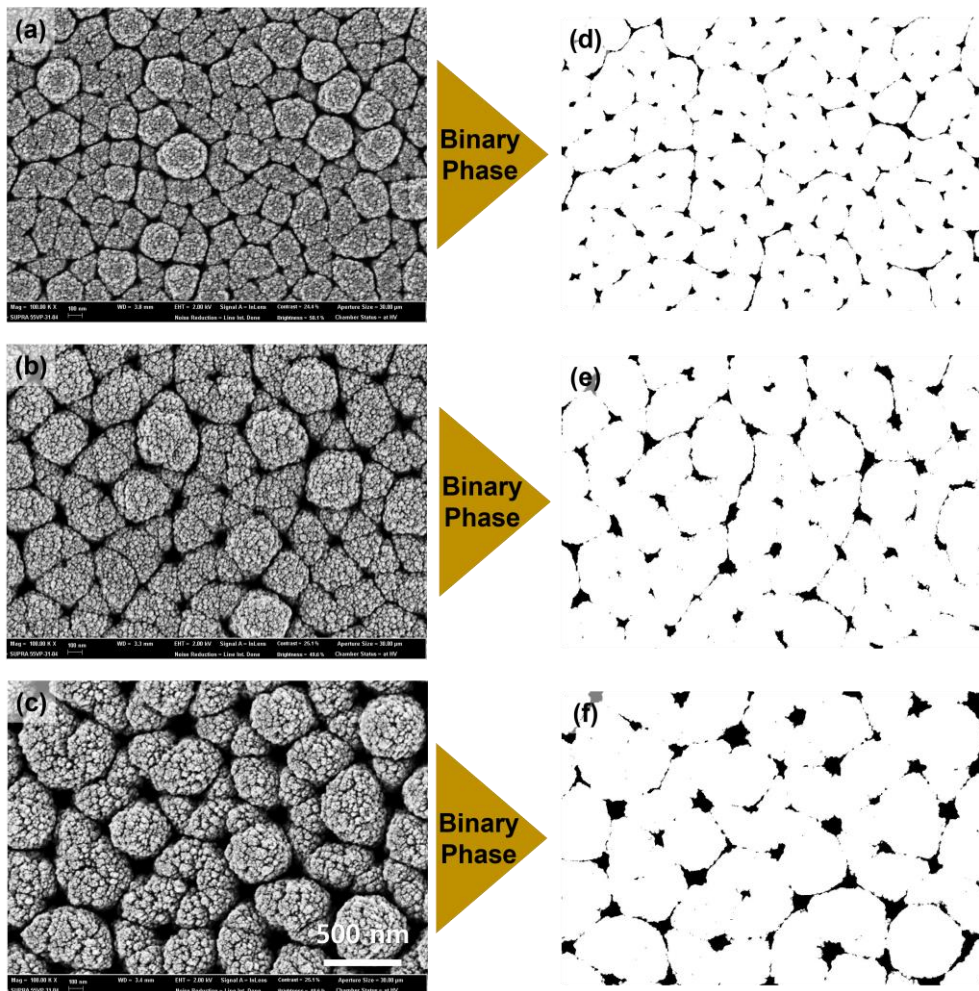


Figure 2-4. Surface images and their binary phase formatted images of Ni-YSZ electrode deposited on AAO80 (a, d), AAO160 (b, e), AAO250 (c, f). All images are in same scale.

film thicknesses of the electrodes on AAO80 (450 nm) and AAO160 (800 nm) are different, their porosity is quite similar. As can be seen in figure 2-4. (d) and (e), each pore of AAO80 cell has a much smaller size than AAO160 cell. However, its density is much higher due to the smaller grain size of the AAO80 cell. Comparing AAO160 and AAO250 cells, the latter has much larger pores. The analyzed value of porosity (10.0%) supports this fact. Those pores surrounded by grains arranged in hexagonal forms come straight from the inherent pores of AAO templates shown in figure 2-2. Straight pores can be secured in this AAO-thin film format. It ensures smooth steam access as fuel to electrolysis and prevents locally concentrated steam due to dead pores.

These cells have gone through electrochemical tests to verify whether microstructural difference by each AAO template affects RSOC performance. The tests were executed at 500°C, feeding the cells with 100 sccm of H<sub>2</sub>O/H<sub>2</sub> (50:50) mixture. Voltage was swept from 0.3V to 1.7V by 10mV of step size and 25mV/s of scan rate (figure 2-5. (a)). The open circuit potential of each case reflects the microstructure, or porosity, as confirmed with figure 2-4. AAO80 and AAO160 cells OCV exceed 1.0 V, while that of AAO250 cell is below 1.0 V (0.99 V). This is due to the higher porosity of the Ni-YSZ fuel electrode on the AAO250 template. Large porosity

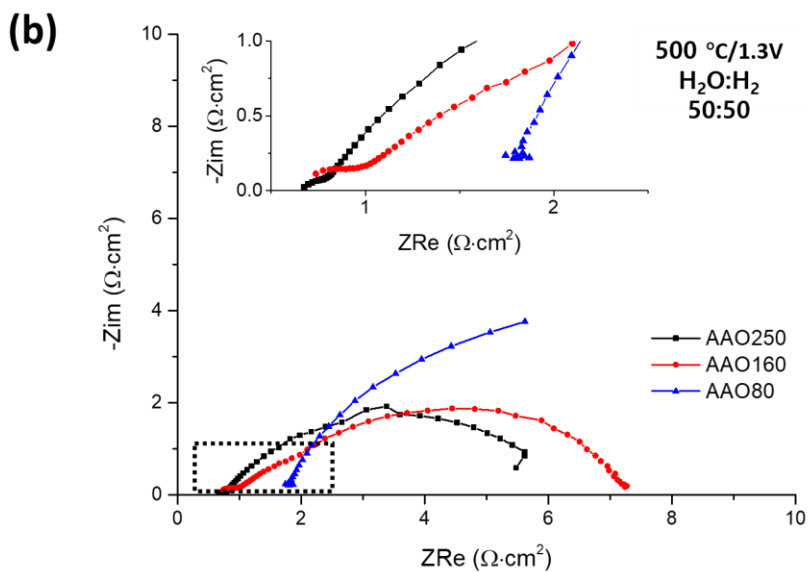
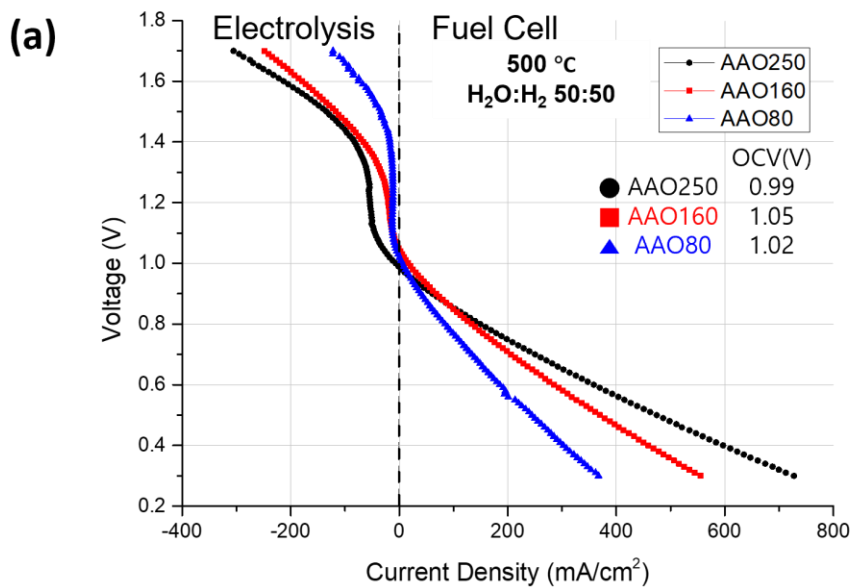


Figure 2–5. Electrochemical characterization of cells deposited on different AAO templates. (a) Voltage sweep and (b) EIS Nyquist plot at 1.3 V

may induce pinholes in the electrolyte or hinder the electrolyte from fully densifying. Thereby, it brings about decreased OCV values [47]. Apart from porosities, a high steam ratio in the fuel gas thermodynamically derives lower OCV regardless of the cell's structure due to diluted hydrogen [7].

Other than OCV, there is a significantly noticeable difference between each cell. It is noteworthy to compare AAO80 and AAO160, or AAO160 and AAO250. AAO80 and AAO160 have similar porosity values, as confirmed in figure 2–4, despite their different Ni–YSZ thickness and average pore size of AAO templates. However, it resulted in somewhat different electrochemical performance. For fuel cell mode, 474.5 mA/cm<sup>2</sup> was achieved by AAO250 cell at 0.5V, while 369.6 and 244.6 mA/cm<sup>2</sup> were achieved by AAO160 and AAO80 cells at 0.5V, respectively. The AAO160 cell outperformed by 51% over the AAO80 cell. Not only in fuel cell mode, but electrolysis mode is also critically affected by the pore size. At 1.3V, thermo–neutral voltage, the current density of the AAO160 cell was 33.1 mA/cm<sup>2</sup>, while that of the AAO80 cell was 12.2 mA/cm<sup>2</sup>. The AAO160 cell has a 2.7 times higher current than the AAO80 cell. Even at 1.7V, the AAO160 cell generated hydrogen two times more than the AAO80 cell (248 and 122 mW/cm<sup>2</sup>). It implies that support with larger pores greatly enhances electrolysis

performance. This trend can be found when comparing the AAO160 cell and the AAO250 cell. The AAO250 cell surpassed the AAO160 cell at both 1.3V and 1.7V by 78% and 23%, respectively. However, they have the same thickness of Ni-YSZ, larger pores, and higher porosity, attributed to enlargement of TPB sites in the fuel electrode and smooth supply of H<sub>2</sub>O/H<sub>2</sub> mixture.

For systematic analysis on where the loss comes from, EIS. The Nyquist plot was measured at 1.3V (figure 2-5. (b)). It confirms that the AAO250 cell has the smallest polarization impedance (4.49  $\Omega \cdot \text{cm}^2$  for AAO250, 6.2  $\Omega \cdot \text{cm}^2$  for AAO160), which can be attributed to the agile charge transfer reaction in the steam electrode. Ohmic resistance, the x-axis intersection in the high frequency region, of AAO250 and AAO160 are identical. Although the porosity of the AAO250 cell is higher, its bigger grain size mitigated this effect, thereby achieving an equivalent ohmic resistance despite its higher porosity.

## 2.4. Conclusion

This chapter investigated the effect of different specifications of AAO templates on the reversible operation performance of solid oxide cells. It turned out that an AAO template with the largest

average pore size has the lowest polarization impedance at 500°C and 1.3V, confirmed by the EIS Nyquist plot. It is attributed to the highest porosity of the Ni-YSZ steam electrode coming from the supporting structure, AAO250. It facilitated smooth steam supply in the steam electrode so that bottlenecks for hydrogen evolution reaction can be alleviated. Not to mention the higher thickness of the electrode, ohmic resistance was significantly enhanced compared to the AAO80 cell because of larger grains of Ni-YSZ. Therefore, it is concluded that the AAO250 template will be used in the following chapters to engineer thin-film reversible solid oxide cells operating at low temperatures.

### 3. Development of Ni–YSZ Steam Electrode and Its Functional Layer

#### 3.1. Introduction

Cermet electrode, the most widely serving electrode type for SOFC and SOEC, has its prime merits in evenly distributed TPBs. It alleviates the bottleneck of adsorption and dissociation of reactants in hydrogen oxidation or hydrogen evolution reactions [48, 49]. Therefore, the dispersed distribution of TPBs and interconnection of each phase is a critical factor for cermet electrode requirement.

The steam electrode of SOEC suffers from Ni relocation in the cathode/electrolyte interface and volatile  $\text{Ni}(\text{OH})_2$  species formation [13]. It primarily occurs when operated in long-term at higher operating temperature (over 700 °C) [23]. To avoid these phenomena, this study previously stated in the introduction that

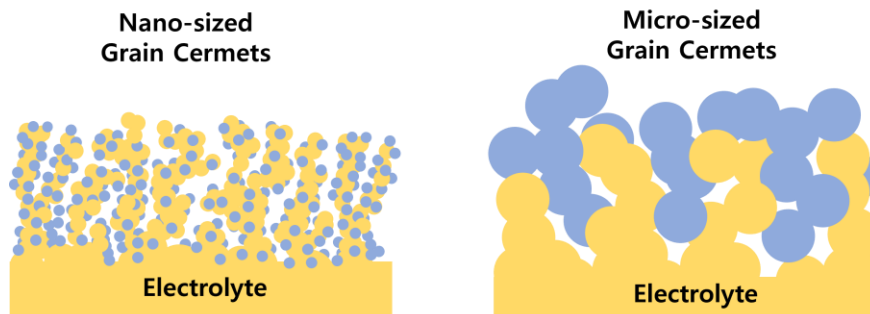


Figure 3–1. Schematic illustrations of cermet electrodes composed of nano–sized grains and micro–sized grains.

straight and columnar structured steam electrodes must be developed to reduce steam concentration gradient significantly.

Since thin films deposited by the sputtering process have nano-sized grains, the sputter-deposited electrode can be an excellent alternative for the cermet electrode fabrication process. By adopting the co-sputtering method, which deposits two or more materials simultaneously using multiple sputter guns, cermet electrodes, such as Ni-YSZ, with dispersed nanograins, can be fabricated (figure 3-1). Cermet electrodes deposited through the co-sputtering method exhibit outstanding electrochemical performance as well. Ionov et al. reported power density increase of a cell with co-sputter deposited Ni-YSZ as high as twice compared to another cell with brush painting fabricated Ni-YSZ [50]. A study by Lee et al. achieved superior maximum power density,  $1.7 \text{ W/cm}^2$  at  $600^\circ\text{C}$  with co-sputtered Ni-YSZ electrode deposited on AAO nanoporous templates [30]. Lim et al. fabricated a Ni-SDC cermet electrode for thin-film SOFC, and its maximum power density surpassed that of the cell with Pt anode [37].

The typical constitution of the conventional anode-supported SOFC has an anode functional layer. The anode support layer has much coarser and bigger grains, while the functional layer has more

refined and smaller grains to extend TPB length at the anode/electrolyte interface [51, 52]. However, the conventional fabrication process requires multiple slurry preparation, application, and high temperature sintering to construct anode layer and anode functional layer composites.

The co-sputtering process can propose a solution to the time-consuming fabrication process for anode and anode functional layer composites. While the conventional process requires a substantial amount of sintering duration at a temperature over 1000°C, electrodes deposited by the sputtering method do not demand a sintering procedure. Furthermore, it can fabricate the component as fast as a few micrometers per hour [53]. Therefore, utilizing the co-sputtering method to fabricate steam electrodes and its functional layer possesses meaningful merit in saving process time and energy. In addition, there is an electrochemical advantage of having nano-sized grains in terms of engineering the cells. Kim et al. fabricated gradient Ru-SDC electrode for direct-methane fueled SOFC via co-sputtering method [54]. Utilizing the benefit of the co-sputtering process, the study fabricated five-sequential layers of gradually changing Ru, Sm, Ce composition within the anode without time-consuming sintering or heat-processing steps.

This chapter comprises the development of high performing Ni-YSZ steam electrode and its functional layer by the co-sputtering process. The Ni-YSZ steam electrode was deposited on an AAO template, and its thickness and various process parameters were investigated. The parameters include substrate rotation speed and sputtering power combination of Ni and Y/Zr. For the functional layer, its Ni and Y/Zr composition was thoroughly examined. Each case's microstructure was observed, and resultant electrochemical performance was measured. FESEM and FIB-SEM were utilized to observe microstructure, while EDS and XPS were exploited to examine the chemical composition of each component. The electrochemical characterization, mainly the  $i$ - $V$  plot and EIS. The Nyquist plot was carried out as well.

## 3.2. Experimental Details

AAO templates with 250 nm of average pore size were used as a support of the thin film SOCs. Various sputtering parameters, including substrate rotation speed, RF sputtering power of Y/Zr target, and total electrode thickness, were adjusted for the steam electrode optimization. The rotation speed of the substrate was varied into two cases: 6.7 rpm and 10.0 rpm. With substrate

rotating at earlier rates, Ni target and Y/Zr (16:84) alloy target were co-sputtered by DC and RF power source, respectively. DC power source was applied to Ni target with a fixed rate of 200W. On the other hand, RF power for sputtering the Y/Zr alloy target was varied. For the steam electrode itself, 25W or 50W was applied. With these parameters, the thickness of the steam electrode was examined into three cases: 800nm, 1200nm, 1500nm. During the process, high purity argon gas was flowed into the chamber to maintain 60 mTorr of the pressure. Target-substrate distance (TSD) was set as 10 cm, and its oblique angle (OA) was 45 degrees.

For the cathode functional layer, the composite of the cathode layer (steam electrode) and its functional layer took up to 850 nm. The cathode layer was deposited for 700nm with 200W of DC power applied to the Ni target and 25W of RF power applied to the Y/Zr alloy target. The functional layer was deposited for 150 nm of thickness. The composition of Ni and Y/Zr was varied by adjusting DC and RF power ratio. Five cases were tried, as shown in table 3-1. During the cathode and the cathode functional layer deposition, chamber atmosphere, TSD, and OA were maintained as described above.

Table 3-1. Detailed process parameters of Ni-YSZ steam electrode composites.

x	Ni-YSZ Single Cathode	Ni-YSZ Cathode Composites					
		Cathode Layer	Cathode Functional Layer				
			N2Y1	N2Y1.5	N2Y2	N1.5Y2	N1Y2
Thickness	800 nm	700 nm	150 nm				
Ni DC Power	200W	200W	200W	200W	200W	150W	100W
Y/Zr RF Power	25W	25W	100W	150W	200W	200W	200W
Atmosphere	Ar 60 mTorr						
TSD	10 cm						
OA	45°						
Substrate Rotation	10 rpm						

All the cases have the same electrolyte and oxygen electrode. The electrolyte was deposited using Y/Zr (16:84) alloy target through a reactive sputtering process. Ar/O<sub>2</sub> (8:2) mixture gas filled the chamber to maintain 10 mTorr of pressure, and the substrate rotated at 6.7 rpm. 200W of RF power was applied to the target, and the final thickness of the electrolyte was 1 $\mu$ m. The oxygen electrode was deposited using Pt target with 100W of DC power applied. The sputtering chamber was maintained at 60 mTorr with high purity Ar gas, and the substrate stayed still. The completed porous Pt oxygen electrode has 450 nm of its thickness.

Fabricated TF RSOCs were electrochemically tested at 500°C, which was increased by 8°C/min of ramping rate. The cells were initially fed with 100 sccm of 3% hydrated H<sub>2</sub> gas during the

temperature ramping. As the cell reached 500°C of operating temperature, 100 sccm of H<sub>2</sub>/H<sub>2</sub>O mixture (50:50 vol.%) flowed into the steam electrode side. The oxygen electrode was exposed to ambient air. I–V plot and EIS analysis were mainly performed. Other than electrochemical tests, microstructure and chemical composition of the cathode composites were carried out. FESEM and FIB–SEM were used for microstructure verification, while EDS and XPS were used for chemical composition investigation.

### **3.3. Results and Discussions**

#### **3.3.1. Determination of Steam Electrode Materials**

This chapter begins with material selection for the steam electrode, where candidates are Ni–YSZ, Ni–GDC, and Pt. Ni–YSZ is the most used steam electrode material combination in solid oxide cells. Not only in SOFC, but it is also widely used SOEC. Ni–GDC steals the spotlight, especially in co–electrolysis or direct carbon–fueled SOFC areas, due to its decent carbon coking prevention properties, although nickel is highly subjected to carbon deposition [55]. Pt is not as massively used materials as the above two, but recently it has been adopted as a catalyst for low temperature SOFC [26, 28, 29, 56].

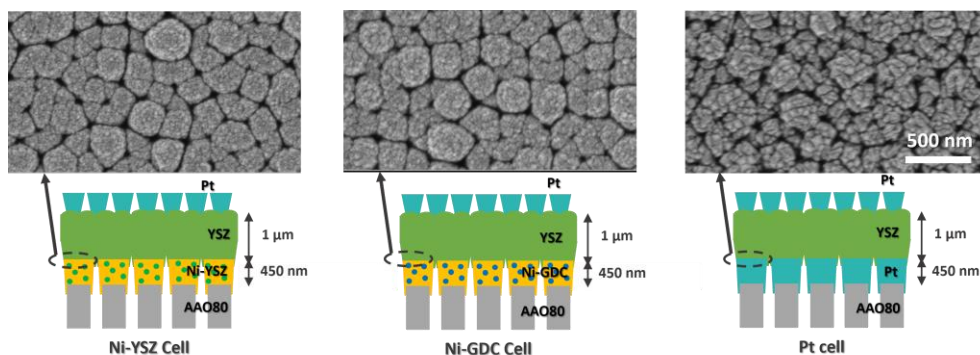


Figure 3-2. Schematic illustrations and surface images of Ni-YSZ, Ni-GDC, and Pt steam electrode deposited on AAO80 templates. All images share the same scale bar.

Ni-YSZ, Ni-GDC, and Pt steam electrodes were deposited on AAO80 substrate to determine an optimal material for RSOC. Their schematic illustrations and surface image of each electrode are depicted in figure 3-2. There is a clear difference between the surface morphology of Pt electrode and Ni-based electrode. However, there is not much difference in surface morphology between Ni-GDC and Ni-YSZ steam electrodes. The thicknesses of the films were set to be 450nm equally.

Electrochemical tests were conducted to investigate the impact of steam electrode material on RSOC performance with identical constitutions. The tests were done at 500°C and 100 sccm of H<sub>2</sub>O/H<sub>2</sub> (50:50) fuel gas. Figure 3-3 (a) shows the voltage sweep of three different cells deposited on AAO80. Although 50 vol.% steam fed the cells, the electrochemical behavior of the cells in the

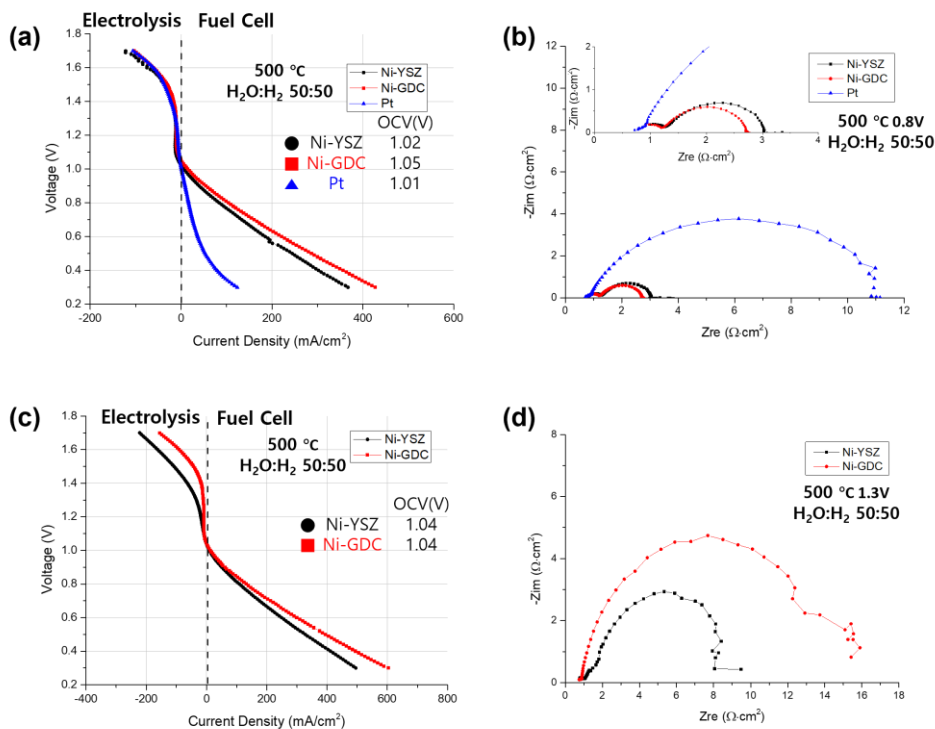


Figure 3–3. Electrochemical tests done with different steam electrode materials. (a) Voltage sweep and (b) EIS spectra at 0.8V of cells with Ni–YSZ, Ni–GDC, and Pt steam electrode on AAO80. (c) Voltage sweep and (d) EIS spectra at 1.3V of cells with Ni–YSZ and Ni–GDC steam electrode on AAO160.

electrolysis region looks like each other, showing poor reversibility, especially at lower electrolysis voltage areas (OCV  $\sim$  1.4V). Shifting interests to fuel cell mode ( $V <$  OCV) shows large discrepancies between Pt and Ni–based electrodes. Ni–GDC cells exhibit slightly better fuel cell performance, achieving 287 mW/cm<sup>2</sup>, while Ni–YSZ cell was 245 mW/cm<sup>2</sup>, which means Ni–GDC cell outperformed Ni–YSZ cell by 17%. This tendency can be confirmed

in EIS. Nyquist plot (figure 3-3. (b)). The Ni-YSZ cell has the largest ohmic resistance,  $1.26 \Omega \cdot \text{cm}^2$ . The Ni-GDC cell show slightly better ohmic resistance,  $1.20 \Omega \cdot \text{cm}^2$ . This can be attributed to a property of GDC, which conducts electrons when exposed to a reducing environment. Not only ohmic resistance but polarization resistance is also lower with Ni-GDC cells. Meanwhile, Pt cell achieved the lowest ohmic resistance,  $0.72 \Omega \cdot \text{cm}^2$ . As it is a pure metal, unlike other cermet materials, it has its strength on ohmic resistance.

Ni-GDC and Ni-YSZ cells were further investigated with a platform of AAO160 (figure 3-3. (c) and (d)). With the AAO160 template, Ni-GDC still outperforms Ni-YSZ cells in fuel cell mode, which was ascribed to GDC's electron conduction property. However, a Ni-YSZ steam electrode cell has much better reversibility in the electrolysis mode. To deeply look into it, this time EIS. Nyquist plot at 1.3V was brought. Due to limited current density at 1.3V, both cells have very high total impedance. But, in detail, Ni-YSZ has much lower polarization resistance compared to Ni-GDC cells. Sciazko et al. reported that the Ni-GDC steam electrode showed more severe degradation in polarization resistance than the Ni-YSZ electrode in SOEC operation [57]. Although the data in figure 3-3. (d) is not from long-term operated

data, Ni-GDC electrode showed worse performance in electrolysis operation.

### 3.3.2. Optimization of Ni-YSZ Steam Electrode

Since this study aims to develop thin film solid oxide cells for reversible operation, Ni-YSZ was chosen to be further examined as it has better reversibility. This section is dedicated to optimizing the Ni-YSZ electrode in chemical composition and microstructure.

First, the composition of Ni-YSZ cermet must be determined. Table 3-2 shows the atomic concentration of Ni-YSZ cermet deposited with Ni 200W-Y/Zr 25W (NY25) and Ni 200W-Y/Zr 50W (NY50). Each cermet shows very high nickel content, although its power ratio is 4:1 in the case of NY50. Their surface microstructure is shown in figure 3-4. Even though their composition difference is only a few percent, their surface morphology is quite different. NY50 cells look more compact. Grains of NY50 has grown enough that their growth is hindered from adjacent grains, forming an energetically most favorable honeycomb structure. On the other hand, NY25 cells appear to have more room to grow. Each grain still maintains a circular shape, clearly different from the NY50 form.

Table 3–2. XPS analysis result of NY25 and NY50 thin films.

Element	NY25	NY50
Ni	70.4%	62.2%
Y	0.1%	0.6%
Zr	0.3%	3.0%
O	21.1%	26.4%
C	8.1%	7.8%
Ni:YSZ	99.5:0.5	95.0:5.0

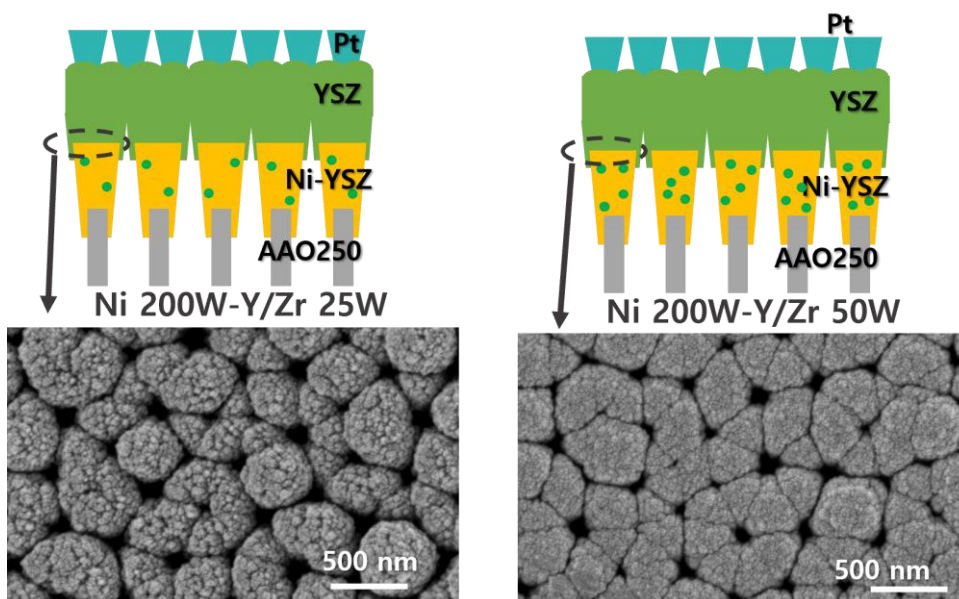


Figure 3–4. Schematic illustrations and surface image of NY25 and NY50 cells.

The electrochemical performances of these cells were compared with each other at 500°C. In the fuel cell mode, it seems NY50 performs better. However, considering that the difference in OCV is about 0.06V, if the curve is re-plotted as current density vs.

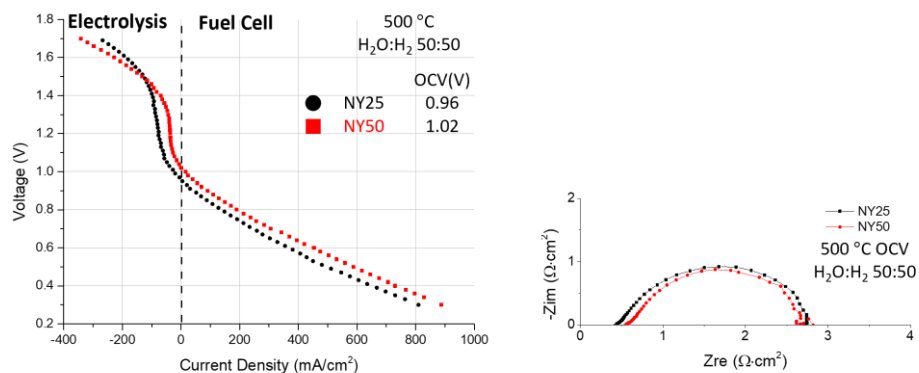


Figure 3-5. Electrochemical test results of NY25 and NY50 cell on AAO250 templates.

overpotential, it is not a significant discrepancy. On the other hand, in electrolysis mode with overpotential corrected, there is a noticeable gap between two cells at or over 1.5V. NY50 cell exceeds NY25 cell in this area, while current densities at low overpotential (OCV  $\sim$  1.4V) are similar. This bottleneck at low overvoltage comes mainly from electrolyte or oxygen electrodes. EIS. Nyquist plot verifies better activity of the NY50 cell. Faradaic resistance of NY50 is smaller than NY25 for about  $0.3 \text{ } \Omega \cdot \text{cm}^2$ . On the other hand, NY25 has better conductivity than NY50, having  $0.1 \text{ } \Omega \cdot \text{cm}^2$  smaller ohmic resistance. This is attributed to the higher nickel composition of the NY25 steam electrode. On the contrary, lower nickel composition, i.e., higher YSZ ratio, yielded a higher density of TPB sites. It resulted in smaller polarization resistance,

as shown in figure 3–5. Furthermore, the more packed microstructure of NY50 acts as a stable base for electrolyte deposition. Thereby, the cell was able to achieve higher OCV. Both electrodes perform well, and the difference is slight, so some parts used the NY25 electrode in this study. In chapter 6, combining all the optimized components at once, the NY50 electrode was used.

With the NY25 electrode, more optimization was carried out, including thickness and sputtering substrate rotation speed. Figure 3–6 shows a surface image of the NY25 electrode by different

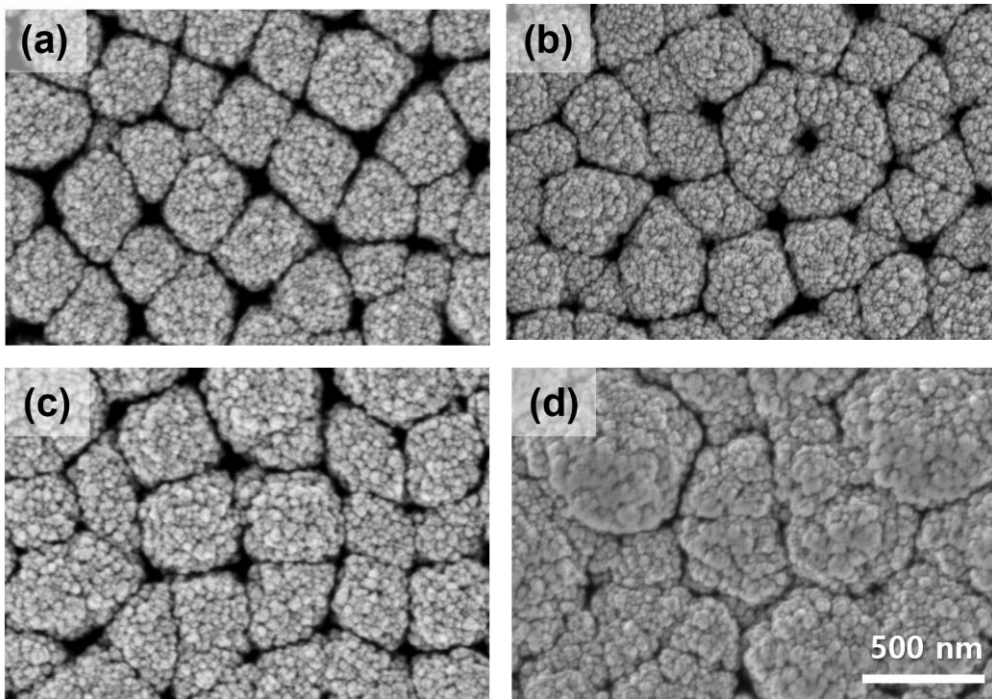


Figure 3–6. Surface FESEM image of NY25 electrode by thickness deposited on AAO250 substrate. (a) 800nm, (b) 1000nm, (c) 1200nm, (d) 1500nm.

thicknesses, ranging from 800nm to 1500nm. As thickness grows, porosity becomes lower.

Those cells with different thicknesses were electrochemically tested and shown in figure 3–7. Thickness with 1000nm achieved the best performance, 626 mA/cm<sup>2</sup> at 0.5V. Its reversibility outperforms others, achieving 259 mA/cm<sup>2</sup> at 1.6V. Ni–YSZ with 800nm thickness had the lowest OCV, probably due to its higher porosity induced YSZ electrolyte to be vulnerable. Then, Ni–YSZ with 1200nm and 1500nm follows, with 1500nm cell's current density decreased significantly.

The tendency can be confirmed with the EIS Nyquist plot in figure 3–7. (b). The Nyquist plot was measured at 500°C and OCV with 100 sccm of H<sub>2</sub>O/H<sub>2</sub> (50:50) mixture fuel input. The 1500 nm cell has the highest faradaic impedance, about 7 Ω·cm<sup>2</sup>, which is ascribed to too much dense architecture blocking the formation of the TPBs. Understandably, 1000nm cell achieved the lowest faradaic resistance, 2.5 Ω·cm<sup>2</sup>. It achieved good intergranular connection and proper density of TPBs to achieve the lowest polarization resistance.

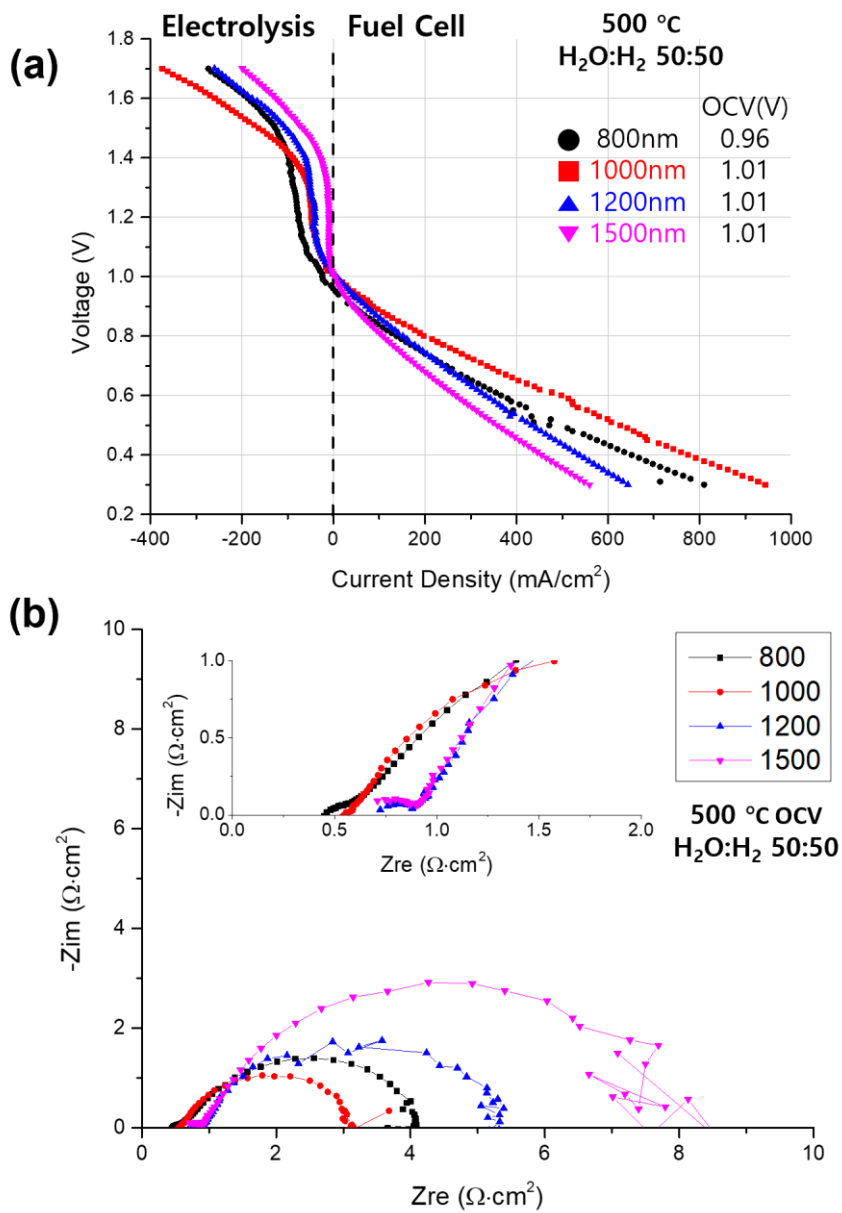


Figure 3–7. Electrochemical tests for Ni–YSZ steam electrode by thickness. (a) Voltage sweep from 0.3V to 1.7V and (b) EIS Nyquist plot measured at 500°C and OCV.

### 3.3.3. Development of Continuous Sputtering Process for Ni–YSZ Cathode Functional Layer

In addition to the cathode optimized in this chapter, the additional functional layer was adopted on top of the cathode. This functional layer was fabricated by a continuous sputtering process, depositing electrode and its functional layer sequentially in a single-chamber process. By simply adjusting DC and RF source power, Ni and Y/Zr composition can be modified easily. This is a much more economical and time-saving process to fabricate cathode composites (cathode and cathode functional layer) than conventional sintering-aided processes. Five different cases were examined for the functional layer. The detailed experimental condition for fabricating the functional layer is shown in table 3-1.

Figure 3-8 shows the surface image of cathode functional layers with different compositions. Overall surface morphology seems quite similar; however, in a closer look, it can be recognized that the surface of each grain becomes smoother as the Y/Zr ratio increases. Since the functional layer is only 150nm~200nm thick, deposition of this layer does not dramatically change the morphology. As can be compared between (a) and (b)~(f), its porosity and overall structure did not change that much. Voltage sweep measured at 500°C shows exciting results. It shows

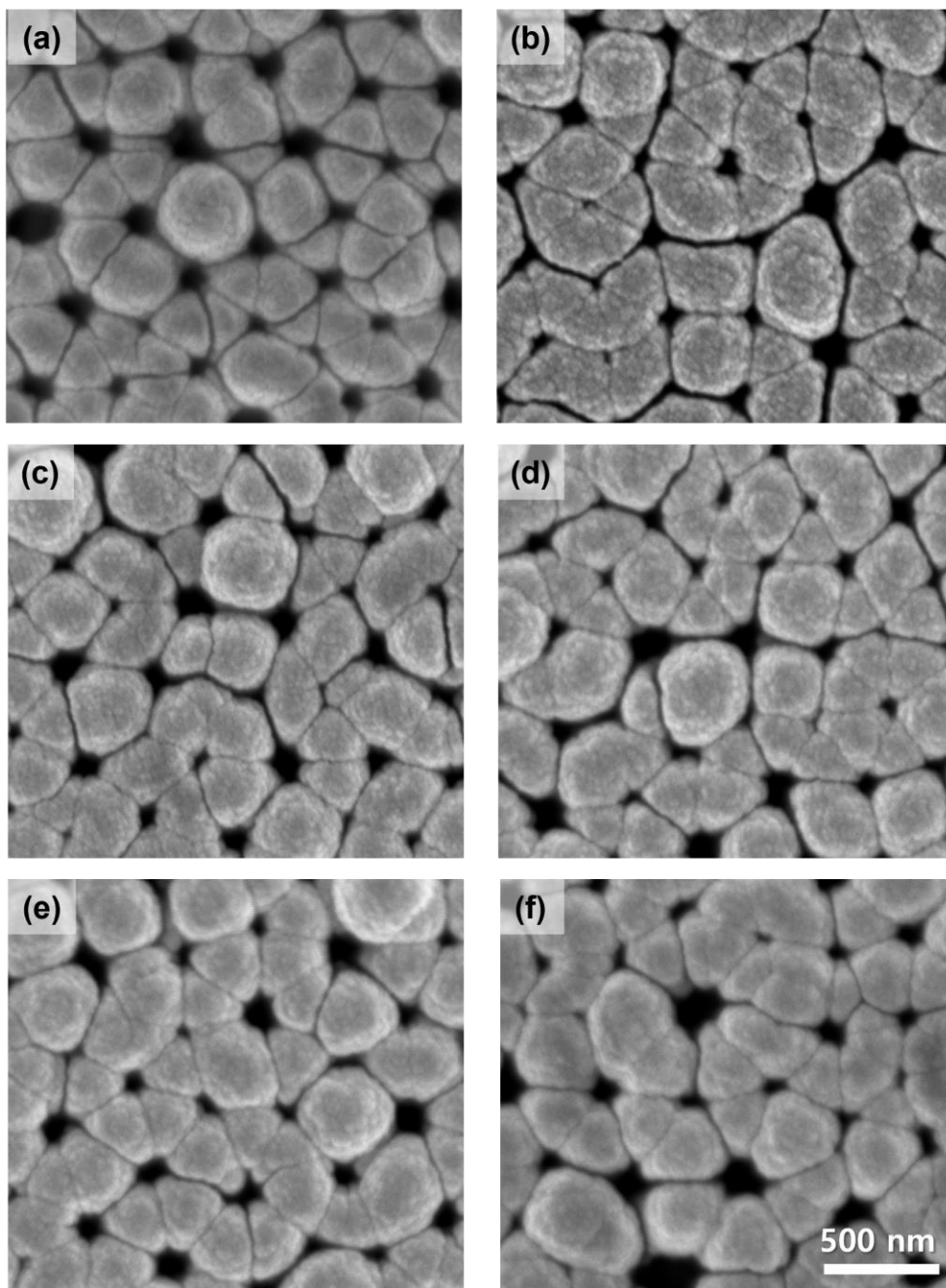


Figure 3–8. Surface FESEM image of (a) Ni–YSZ steam electrode and its functional layers (b–f). (b) N2Y1, (c) N2Y1.5, (d)N2Y2, (e)N1.5Y2, (f)N1Y2

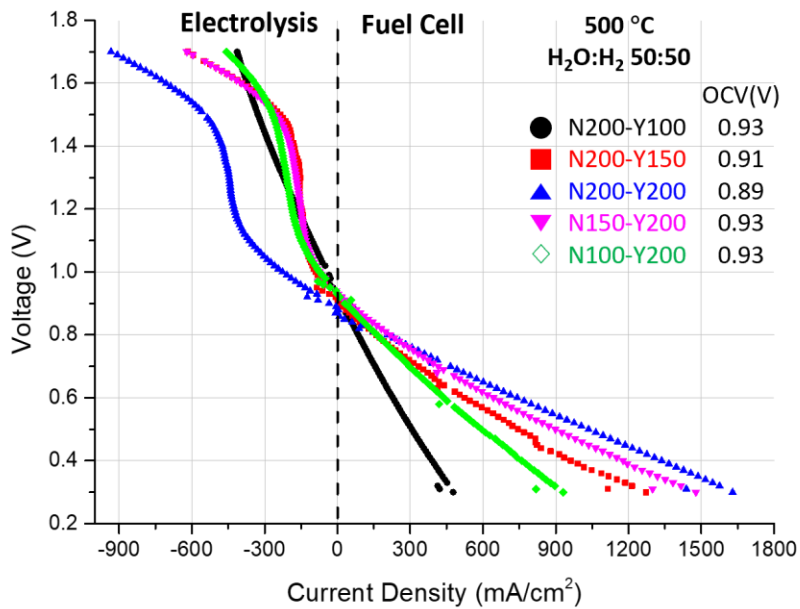


Figure 3–9. voltage sweep curve of cathodic functional layer applied cells measure at 500°C from 0.3V to 1.7V.

N2Y2 cell performed the best among the five. Unlike many others, it even showed much-improved reversibility. This is meaningful because it was achieved only by changing the steam electrode. At 1.3V, the N2Y2 cell reached 446 mA/cm<sup>2</sup>, a significantly improved value compared to the beginning of this chapter.

### 3.4. Conclusion

This chapter mainly investigates steam electrodes to enhance electrochemical performance in SOFC and SOEC mode to have

decent reversibility. Although oxygen electrode or electrolyte/anode interface is the main bottleneck for electrolysis operation[58], optimizing steam electrode only could enhance reversibility a lot. Specifically, the current density at 1.7V increased by 231% by optimizing the Ni-YSZ steam electrode and introducing a functional layer.

## 4. Optimization of YSZ Sputtering Process

### 4.1. Introduction

The electrolyte is one of the most critical components in solid oxide fuel cells and electrolyzer cells. It plays multiple parts, such as separator, ion conductor, reaction sites, and even support in some cases [7, 59]. It is exposed to both oxidizing and reducing environments on each side simultaneously, and it must be dense and pin-hole-free to block fuel crossover sufficiently. Thus, researchers worldwide have spent lots of effort to secure robust, durable, and high-performing solid electrolytes over decades.

In SOEC, there are multiple issues regarding electrolytes. Inter- or intra-granular pore formation can be observed with the cells mainly operated at high temperatures ( $>800^{\circ}\text{C}$ ), and high potentials applied [20–22]. Therefore, the most efficient measure to overcome these problems is to operate at lower temperatures ( $<600^{\circ}\text{C}$ ), as previously stated in chapter 1.

However, the most critical point when the cells operated at a lower temperature is the decrease of ionic conductivity (figure 4–1) and chemical reaction activity. Nonetheless, considering resistance proportional to the length of the conduction path,

shortening the conduction path would decrease the loss coming from low ionic conductivity. Shortening the conduction path means making electrolytes thinner. In recent years, it has been attempted with the benefit of vacuum-assisted equipment to achieve sub-micron electrolytes [28, 35, 60, 61]. Furthermore, sluggish interface reactions in low temperatures can be fixed with the improved interfacial property. Ryu et al. discovered about 50 nm of additional 3D-structured YSZ Layer enhanced ORR activity and consequentially improved the maximum power density by 30% [62].

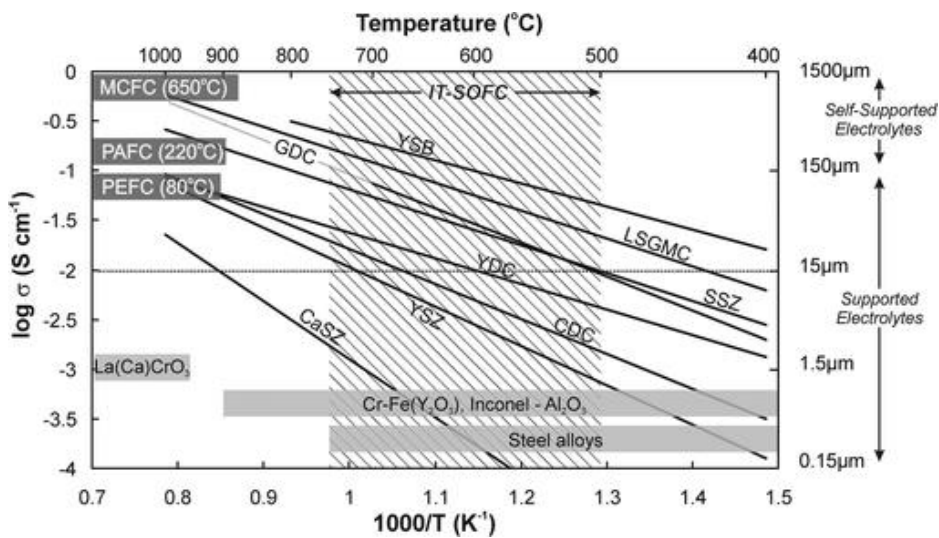


Figure 4-1. Ionic conductivity of selected solid oxide electrolyte materials as a reciprocal temperature function [63].

This chapter is dedicated to developing high-performing YSZ electrolytes with 1  $\mu\text{m}$  thickness. To fulfill this, various process parameters were investigated, such as target-substrate distance

(TSD) and substrate rotation speed. Ni–YSZ single electrode was utilized as a steam electrode, and porous platinum was deposited on top of the electrolyte as an oxygen electrode. Finally, the electrochemical test was performed to see its performance as RSOC. By adjusting the TSD and rotation speed of the sputtering process, the cell's reversibility and water electrolysis performance improved much better, exceeding  $1\text{A}/\text{cm}^2$  at  $1.3\text{V}$  and  $500^\circ\text{C}$ . Additional analyses, including FESEM, FIB–SEM, AFM, TEM, XRD, and XRR, were performed to investigate the YSZ thin films.

## 4.2. Experimental Details

All the components were kept the same except electrolyte. AAO template with  $250\text{ nm}$  of average pore size and  $1 \times 1\text{ cm}^2$  of the area was used as a support. Ni–YSZ steam electrode was deposited on the support by applying  $200\text{W}$  of DC power on Ni and  $25\text{W}$  of RF power on Y/Zr. The chamber atmosphere was kept at  $60\text{ mTorr}$  of pure Ar gas during the sputtering process. The thickness of the steam electrode was set as  $800\text{ nm}$ . On the electrolyte, porous Pt anode was deposited by DC magnetron sputtering.  $100\text{W}$  of DC power was applied, and the sputtering chamber was filled with  $60\text{ mTorr}$  of high purity Ar gas. The thickness of the Pt oxygen electrode reached about  $400\text{ nm}$ .

YSZ electrolyte was deposited into four cases based on target–substrate distance (TSD) and substrate rotation speed (SRS). Each variable has two cases, combining their results in four separate cases. For the TSD, there are reference cases (13cm), and 3 cm reduced cases. Substrate rotation speed was set as 6.7 rpm and 10.0 rpm. The whole cases were numbered, as shown in table 4–1. The chamber was filled with 10 mTorr of Ar/O<sub>2</sub> (8:2) mixture gas during the reactive sputtering process. 200W of RF power was applied to Y/Zr (16:84) alloy target, and the deposition was done at room temperature. All the cases reached their thickness at 1 $\mu$ m.

The microstructure of the deposited YSZ was investigated with FESEM, FIB–SEM, and AFM. Its crystallinity and film density were examined by XRD and XRR analysis. TEM analysis was conducted

Table 4–1. Detailed experimental condition for each deposition cases.

Cases	TSD	SRS	RF Power	Atmosphere	Thickness
13L	13cm	6.7 rpm	200 W	10mTorr Ar/O <sub>2</sub> (8:2)	1 $\mu$ m
13H	13cm	10.0 rpm			
10L	10cm	6.7rpm			
10H	10cm	10.0 rpm			

to study the change in the atomic scale variation caused by process parameters. The detailed procedures of electrochemical characterization are described in the previous chapter.

### 4.3. Results and Discussions

YSZ electrolyte deposited on Ni-YSZ steam electrode by substrate rotation speed (SRS) and target-substrate distance (TSD) variation was observed via FESEM as shown in figure 4-2. Decreasing the TSD value resulted in packed surface morphology,

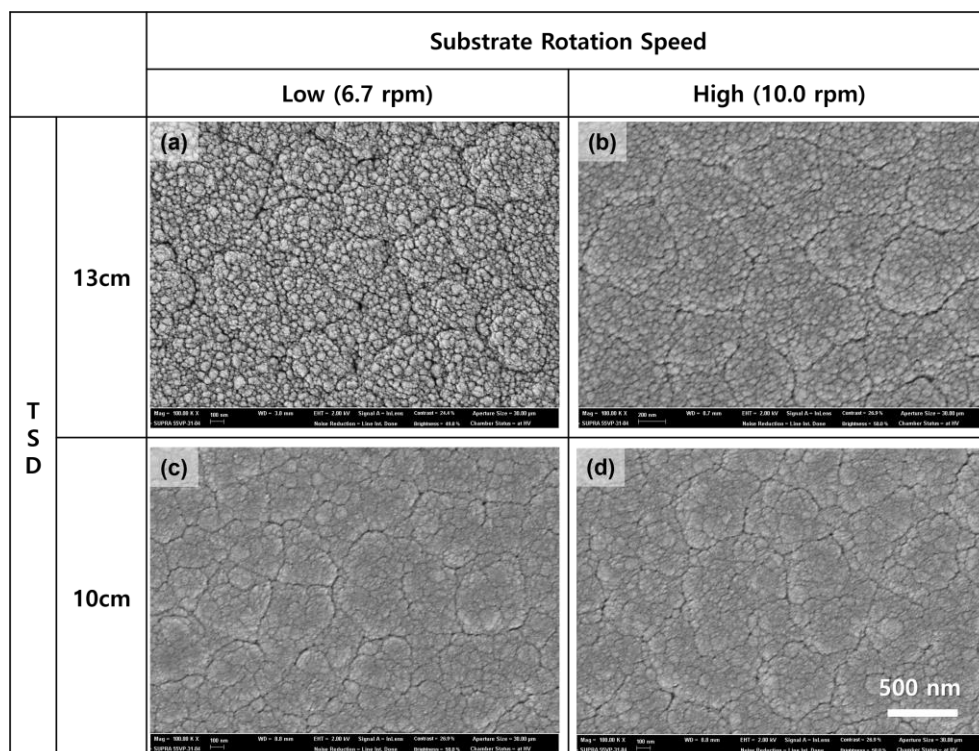


Figure 4-2. FESEM surface image of YSZ electrolyte deposited in various condition on Ni-YSZ steam electrode.

as

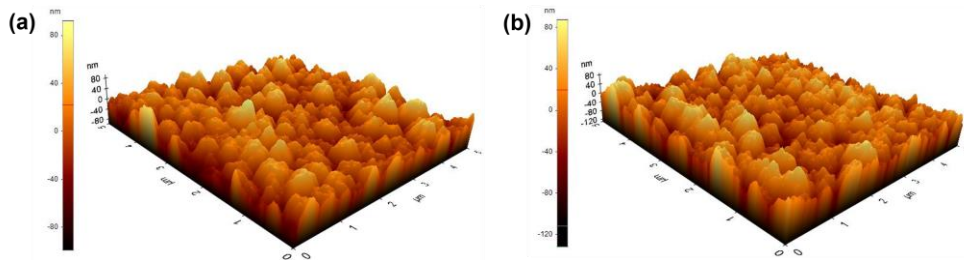


Figure 4-3. 3D Topographic image of YSZ taken by AFM analysis. (a) 13L and (b) 13H.

seen in (c) and (d). Comparing (a) and (b), rotating the substrate at a higher rate seems to affect the surface morphology in some way, but it cannot be figured out through just the image. Therefore, AFM analysis was carried out for 13L and 13H electrolytes as shown in figure 4-3. AFM analysis was carried out with terrain correction method to exclude inherent roughness of original support and to solely investigate YSZ thin film. Root mean square values for surface roughness are 24.128 nm for 13L YSZ (figure 4-3. (a)) and 26.460nm for 13H YSZ (figure 4-3. (b)). It turned out that 13H YSZ has 9.7% higher surface roughness.

Crystallinity of each case was investigated by means of XRD analysis (figure 4-4). XRD measurement was done with grazing incidence (GI.) XRD. All the films have four discrete peaks, but their intensities are different. Comparing TSD, variation of YSZ, reducing TSD from 13cm to 10cm produced weaker intensity of (111). It corresponds to both SRS (13L to 10L, 13H to 10H), while

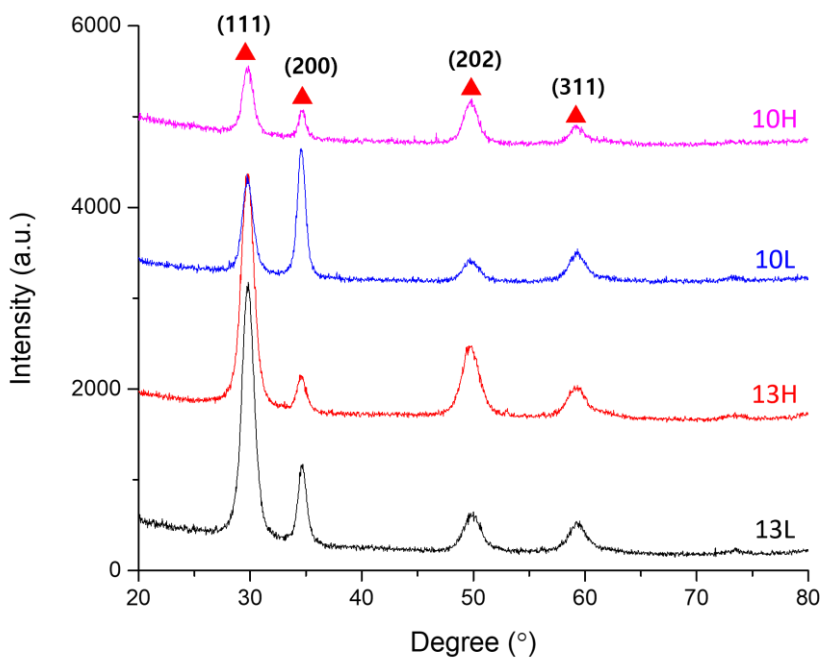


Figure 4-4. XRD analysis of different YSZ films deposited on Si wafer.

other peaks intensity shows not much difference. Therefore, (111) peak is the most affected peak by TSD. adjustment. On the other hand, controlling SRS bring about interesting results as well. By increasing the SRS (13L to 13H or 10L to 10H), (200) peak shrinks, while (202) peak become intensified. Therefore, comparing 13L and 10H, reducing TSD from 13cm to 10cm yielded decrease of (111) peak, and increase of SRS from 6.7rpm(L) to 10.0rpm(H) resulted in weakened (200) peak and intensified (202) peak. In short, highly oriented film of 13L converted into evenly oriented, nanocrystalline

film of 10H.

Using these electrolytes, electrochemical tests were carried out at 500°C (figure 4–5). From 13L YSZ, as TSD was shortened and SRS increased, reversible electrochemical performance become better. In fuel cell mode, at 0.5V, 13L YSZ cell produced current density of 622 mA/cm<sup>2</sup>, while 10H YSZ cell achieved 1478 mA/cm<sup>2</sup>, about 2.4 times higher. Its performance enhanced in SOEC mode as well. Interestingly, all cases except 10H YSZ had difficulties in electrolysis operation. This phenomenon is analogous to previous chapters. It was inferred that since the main obstacle for SOEC is oxygen evolution reaction, improving oxygen electrode would only improve SOEC operation meaningfully. However, improving electrolyte and electrolyte/anode interface, reversibility and SOEC operation enhanced significantly as shown in figure 4–5 (a). At 1.3V, 13L YSZ sample consumed merely 51 mA/cm<sup>2</sup> to produce hydrogen, whereas 10H YSZ case achieved 964 mA/cm<sup>2</sup>, achieving 19 times higher hydrogen consumption rate at thermoneutral voltage. This value, nearly 1A/cm<sup>2</sup> at 500°C and 1.3V, thermoneutral voltage, is the world record by far as far as the author's knowledge.

EIS Nyquist plots explain how each resistance contributed one's

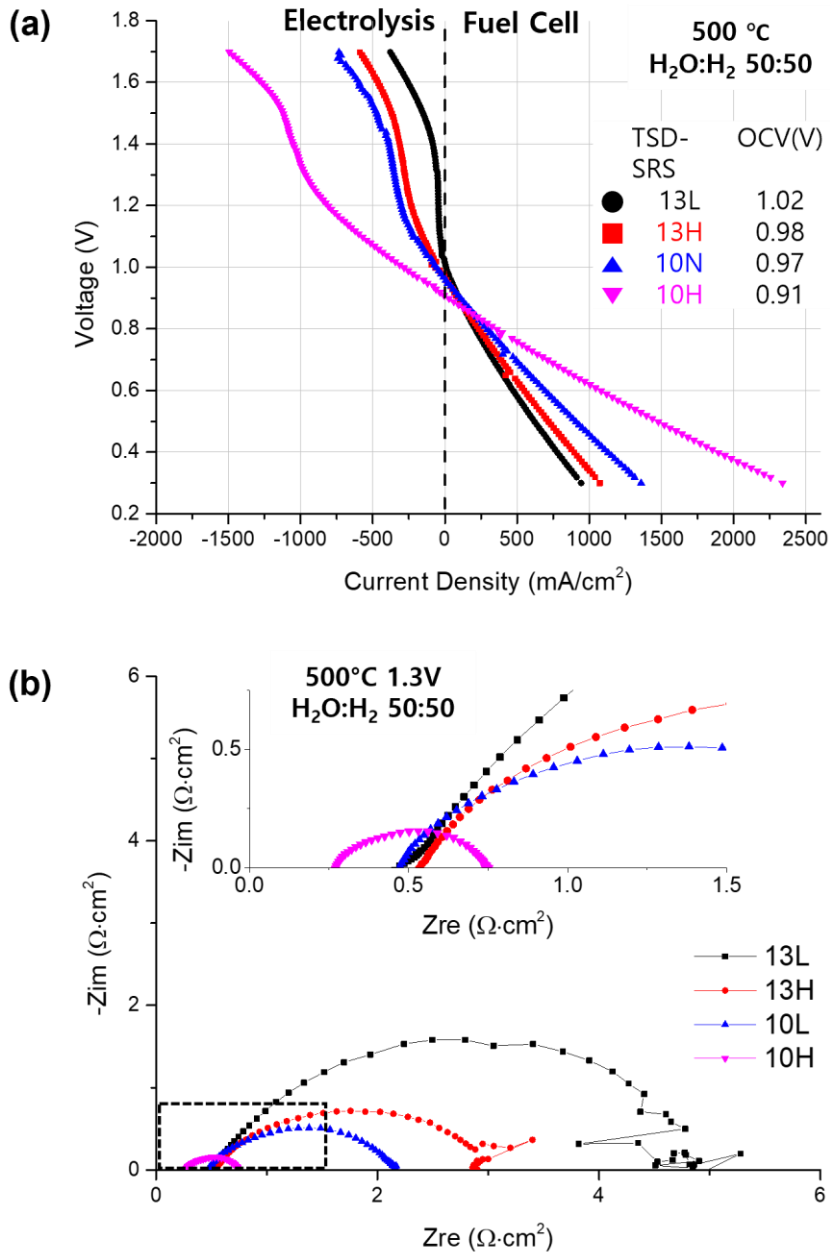


Figure 4–5. Electrochemical characterizations of TSD and SRS adjusted SOCs. (a) Voltage sweep from 0.3V to 1.7V, (b) EIS Nyquist plot at 500 °C 1.3V.

performance. First thing to notice is that 10H case has the smallest ohmic resistance,  $0.26 \Omega \cdot \text{cm}^2$ , while others have similar value around  $0.5 \Omega \cdot \text{cm}^2$ . Assuming there is no difference in ohmic resistance coming from Ni-YSZ cathode and Pt anode, this much low ohmic resistance of 10H YSZ can be attributed to its crystallinity. Its nano-crystallinity contributed better ionic conductivity of electrolyte, thereby lower ohmic resistance was able to be achieved. Furthermore, as discussed with figure 4-2 and 4-3, 10H YSZ has much more packed morphology and higher surface density. Thanks to these attained features, it refined anode/electrolyte interface, which resulted in considerably small polarization impedance. Even without using MIEC materials as oxygen electrode, electrolysis operation could be better by optimizing anode/electrolyte interface.

#### **4.4. Conclusion**

This chapter dealt with YSZ electrolyte in terms of adjusting its fabrication process parameters. The parameters include target-substrate distance (TSD) and substrate rotation speed (SRS) of magnetron sputtering process. By adjusting those parameters properly, YSZ electrolyte could achieve not only nano-crystallinity,

but also enhanced anode/electrolyte interface property. Synergetic effect of these achievements produced outstanding performance of the thin film reversible solid oxide cells. In specific, 0.964 A/cm<sup>2</sup> at 1.3V and 500°C was achieved. This value close to 1A/cm<sup>2</sup> is by far the best achieved current density among reported literatures at 1.3V, as low as 500°C operating temperature. It is noteworthy that this value was achieved by only optimizing YSZ electrolyte using pure metal Pt oxygen electrode.

## 5. Development of LSCF–GDC Oxygen Electrode for Oxygen Evolution Reaction

### 5.1. Introduction

Oxygen electrode is the component where the most severe performance drop occurs in solid oxide cells due to sluggish reaction incorporating oxygen. Researchers in this field have been focused on oxygen electrode for long time. Particularly, oxygen evolution reaction, the reaction takes place when operating in electrolysis mode, causes critical deterioration on SOEC because of its localized generation of oxygen in TPBs, i.e., unbalanced distribution of oxygen partial pressure ( $p_{O_2}$ ) [13, 64, 65]. In SOEC, other factors, such as high anodic potential applied, high operating temperature, and highly tortuous microstructure, are known to exacerbate the degradation.

Since the factors like high anodic potential or operating temperature cannot be easily adjusted depend on operating condition, the one that must rather be changed is microstructure. The strategy to overcome deterioration in oxygen electrode was previously stated in chapter 1 that straight and columnar pore structure must be adopted to alleviate unbalanced local distribution of  $p_{O_2}$ . Furthermore, operating SOEC at lower temperature will

naturally mitigate the degradation in anode/electrolyte interface.

Even conventional materials like LSCF–GDC or LSC–YSZ can exhibit outstanding electrochemical activity as long as adequate microstructure is ensured. Wu et al. adopted honeycomb–architecture LSC–YSZ electrode with low tortuosity factor ( $\sim 1$ ) in SOEC [19]. The cell with newly developed anode achieved the lowest reported polarization resistance of anode and confirmed a few hours of durability at  $2.0 \text{ A/cm}^2$  at  $800^\circ\text{C}$ . LSC– or LSCF–based electrode with straight and columnar pores can be realized with inherent columnar growth tendency of sputtering. Lee et al. fabricated porous columnar LSCF–YSZ oxygen electrode by co–sputtering method and achieved  $1.7 \text{ W/cm}^2$  at  $600^\circ\text{C}$  in SOFC operation [30]. The same research group fabricated LSC–GDC oxygen electrode by co–sputtering as well [43].

In this chapter, LSCF–GDC oxygen electrode was fabricated via co–sputtering method to ensure porous and low–tortuosity profile of microstructure. The electrodes were first implemented on ScSZ pellet to examine its electrochemical performance without any external variables. Optimum composition ratio was determined in terms of its reversibility as RSOC and activity on oxygen evolution reaction. A few candidates were sorted out and applied on AAO–based TF RSOC. The LSCF–GDC anode with the best performing composition was additionally investigated on the

effect of its thickness. Microstructure was confirmed by FESEM and TEM. Its composition was roughly checked via EDS. Crystallinity of the deposited LSCF–GDC films were verified with grazing incidence (GI.) XRD.

## 5.2. Experimental Details

ScSZ((Sc<sub>2</sub>O<sub>3</sub>)<sub>0.09</sub>(ZrO<sub>2</sub>)<sub>0.91</sub>) electrolyte supports with 150 $\mu$ m of thickness and 1cm by 1cm of surface area was utilized to test potential LSCF–GDC electrode combinations. On one side of the support, Ni–YSZ steam electrode was deposited by co–sputtering process. 200W of DC power was applied to Ni target while 25W of RF power was applied to Y/Zr (16:84) alloy target. The atmosphere during the process was kept at 60 mTorr of high purity argon gas and substrate was rotated with the rate of 10.0 rpm. The deposited

Table 5–1. Detailed sputtering parameters for fabricating LSCF–GDC anode.

Nomen- clature	Power		Atmosphere	Substrate Rotation	Configuration
	LSCF	GDC			
100–30	RF 100W	DC 30W	Ar 30mTorr	X	TSD 11cm  OA 60°
100–40	RF 100W	DC 40W			
100–50	RF 100W	DC 50W			
100–60	RF 100W	DC 60W			
100–80	RF 100W	DC 80W			
100–100	RF 100W	DC 100W			
80–100	RF 80W	DC 100W			

Ni-YSZ cathode has 450nm of thickness. On the other side, porous columnar LSCF-GDC anode was deposited with various composition. Ratio of each phase was manipulated by DC and RF power source variation during the co-sputtering process. LSCF phase was deposited using  $(\text{La}_{0.6}\text{Sr}_{0.4})_{0.98}\text{Co}_{0.2}\text{Fe}_{0.8}\text{O}_{3-\delta}$  perovskite target (AEM Deposition, China) via RF power source, of which applied power was fixed at 100W. GDC phase was deposited using Gd/Ce (2:8) alloy target (AEM Deposition, China) via DC power source. By varying the DC power, composition of LSCF-GDC was adjusted. DC power for Gd/Ce deposition was varied as follow: 30, 40, 50, 60, 80, 100W. At DC 100W, 80W of RF power was additionally coupled with. After LSCF-GDC was deposited, 150nm of Pt was deposited using DC magnetron sputtering for the sake of current collection. Table 5-1 summarizes the detailed sputtering parameters for fabricating LSCF-GDC electrode.

Among the composition tried with ScSZ electrolyte supported cells, four cases (<100-40>, <100-50>, <100-60>, <100-80>) were chosen to be adopted on AAO-based cells. On AAO250, Ni-YSZ electrode was deposited with the same condition as chapter 4. Then, YSZ electrolyte was deposited with the identical parameters of chapter 3. Finally, those four cases of LSCF-GDC oxygen electrodes were fabricated on top of the electrolyte, while the

detailed parameters are same as those deposited on ScSZ pellets.

Fabricated electrolyte-supported cells and AAO-supported cells were electrochemically tested at 500°C with 100 sccm of H<sub>2</sub>O/H<sub>2</sub> (50:50) mixture. Detailed parameters for electrochemical characterization conducted in this chapter is same as previous chapters. FESEM was utilized to observe its cross-sectional and surface microstructure. Along with FESEM, EDS analysis was performed to prove homogeneous distribution of LSCF and GDC phase around the anode. XRD was utilized to investigate confirm LSCF-GDC phases in as-deposited and 500°C 1hr annealed condition.

## **5.3. Results and Discussions**

### **5.3.1. Determination of optimum composition on electrolyte-supported cells**

FESEM images of surface and cross-sections of LSCF-GDC thin films were observed to identify each microstructure depend on chemical compositions. By utilizing Gd/Ce alloy targets on DC power source, LSCF-GDC MIEC material can be deposited in columnar-way as shown in figure 5-1. All the compositions show similar morphology. Their grain size depends on thickness of the LSCF-GDC. As the film grows, the grain size become bigger since sputter

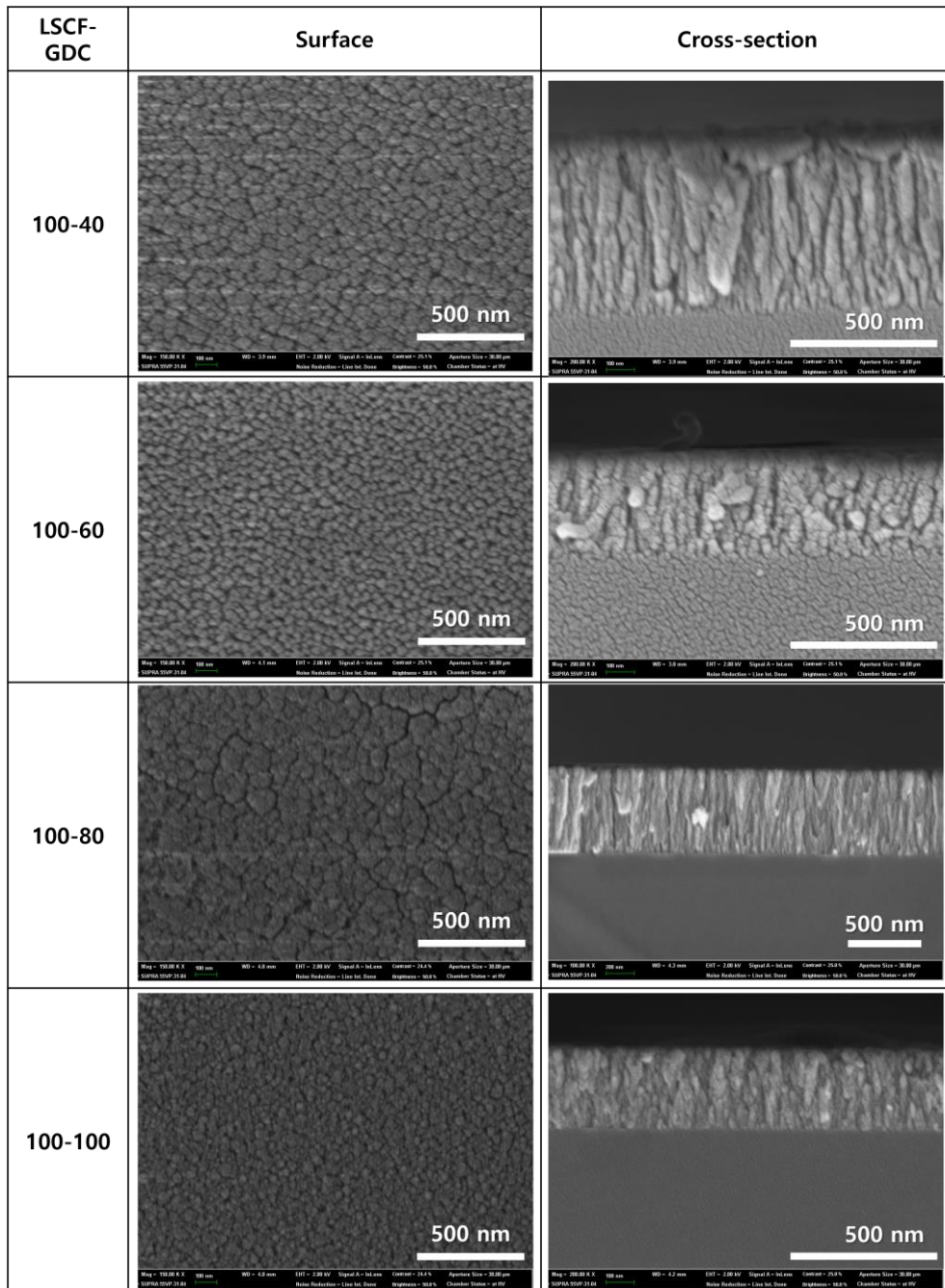


Figure 5-1. Surface and cross-sectional FESEM images of selected thin film LSCF-GDC combination deposited on Si wafer.

-deposited porous films grow in inverted trapezoid forms. Through the images, it was confirmed that all cases with different composition have columnar film architecture, which ensure smooth oxygen dispersion whenever it evolves. This is what this thesis aims to develop as emphasized in chapter 1.

Right composition must be decided based on electrochemical performance. Above combinations of LSCF-GDC MIEC were adopted on ScSZ pellets to investigate its electrochemical performance. Pt oxygen electrode was used for the reference cell. On the other side of the pellet, Ni-YSZ steam electrode was deposited by co-sputtering. The electrolyte-supported cells were

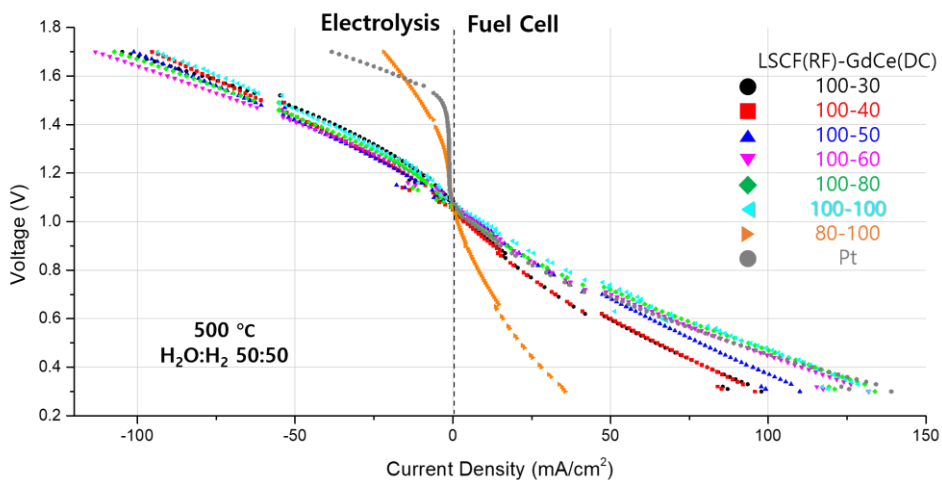


Figure 5-2. Voltage sweep of ScSZ electrolyte-supported cells with oxygen electrode of various LSCF-GDC composition measured at 500 °C. Pt oxygen electrode was used as reference.

then electrochemically tested at 500°C.

A cell with Pt oxygen electrode performs as most other LSCF–GDC oxygen electrode cells in fuel cell mode. However, in electrolysis mode, the cell's electrochemical performance is very poor. It is worse than any other LSCF–GDC oxygen electrode cell. Fuel cell performance of Pt cell is, however, equal to the best performing LSCF–GDC electrode. Therefore, at least in terms of reversibility, thin film LSCF–GDC electrode outstrips Pt oxygen electrode. Among LSCF–GDC oxygen electrodes, cells with RF and DC power combination of <100–80> and <100–60> performed the best in terms of both fuel cell and electrolysis operation. Except <80–100> cell, cells with all composition showed quite comparable reversible performance with each other. Therefore, some of the selected LSCF–GDC combinations were applied on AAO–based thin film RSOC and tested.

### **5.3.2. Determination of optimum composition on AAO–based cells**

The selected LSCF–GDC combinations were adopted on AAO–based cells. As figure 5–3 shows, the cells have great reversibility. In addition, their performance discrepancy is not that dramatic, which is analogous to the previous tests on electrolyte–supported cells (figure 5–2). Among them, the <100–80> cell exhibits best

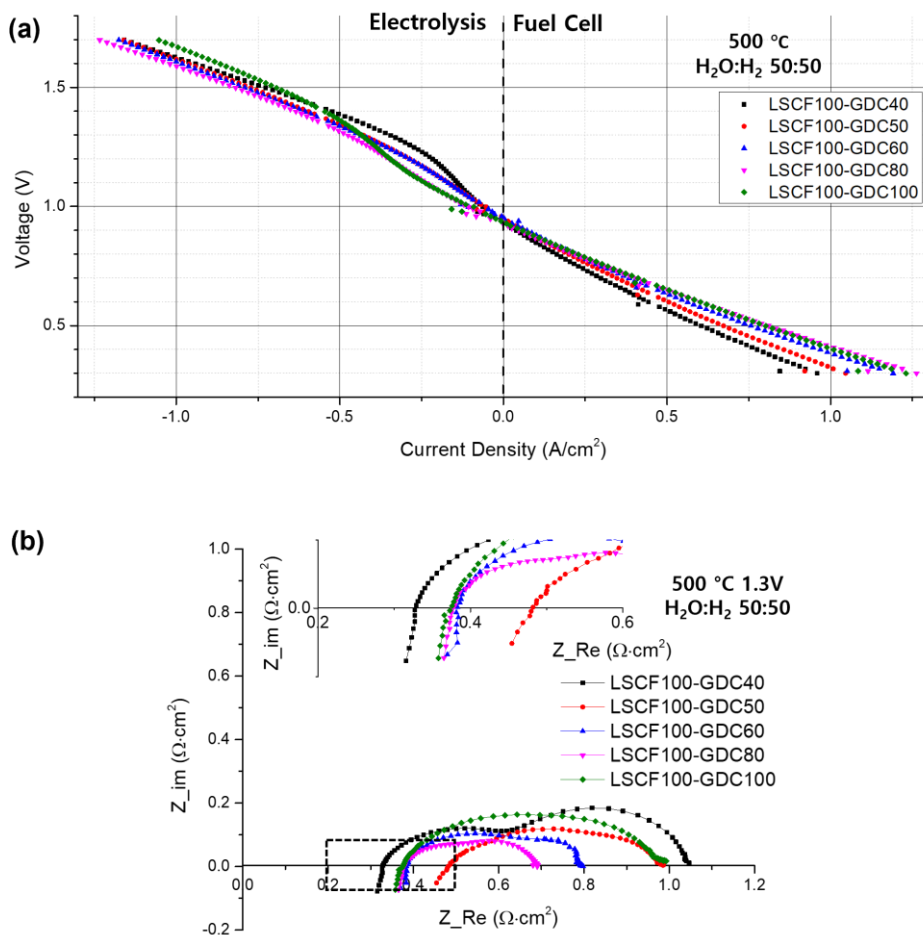


Figure 5-3. (a) Voltage sweep and (b) EIS Nyquist plot of LSCF-GDC anode adopted thin film RSOCs.

performance in both fuel cell and electrolysis operation. This is a different result from the one with electrolyte-supported cells, where <100-60> cell performed the best. Even though the tendency is different, the discrepancy is very small, and all the cells have decent reversibility and performance as well. <100-80> cell

produced  $0.81 \text{ A/cm}^2$  at  $0.5\text{V}$  in fuel cell mode, while it produced hydrogen from  $0.47 \text{ A/cm}^2$  current input at thermoneutral voltage,  $1.3\text{V}$ . The OCV of all of the cells were in the range of  $0.93\sim 0.95 \text{ V}$ .

In EIS. Nyquist plot, it can be easily distinguished that  $\langle 100-80 \rangle$  cell outperformed others. It has the minimal size of polarization resistance,  $0.31 \Omega \cdot \text{cm}^2$ . Furthermore, its ohmic resistance is about  $0.38 \Omega \cdot \text{cm}^2$ . Other cells have larger faradaic resistance than  $\langle 100-80 \rangle$  cell. Interestingly,  $\langle 100-40 \rangle$  cell has lower ohmic resistance value,  $0.33 \Omega \cdot \text{cm}^2$ , than  $\langle 100-80 \rangle$  cell. It is attributed to higher LSCF content, since LSCF is MIEC material that has electronic conduction as well. However, the largest polarization impedance of the cell hindered the cell to become the best-performing cell. This must be due to lack of metallic Gd/Ce phase on as-deposited condition. Metallic Gd/Ce phase during the co-sputtering forms the backbone structure and LSCF homogeneously sits down on the bones.  $\langle 100-40 \rangle$  has less amount of GdCe deposited, thereby not enough to form a discrete backbone. Therefore,  $\langle 100-80 \rangle$  combination of LSCF-GDC was chosen to finally be adopted on.

### **5.3.3. Investigation on Optimum Thickness of LSCF-GDC anode**

$\langle 100-80 \rangle$  cells were fabricated into three different thickness

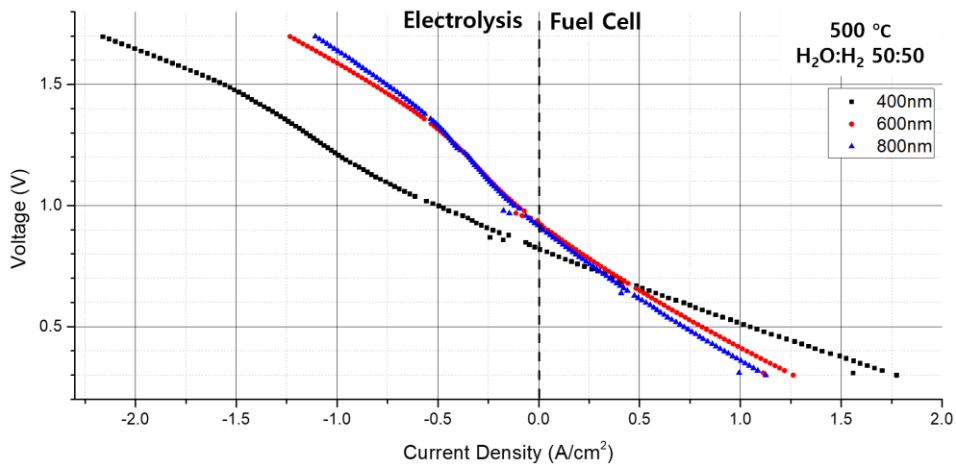


Figure 5-4. Voltage sweep from 0.3V to 1.7V on LSCF-GDC oxygen electrode cells with different thickness.

on AAO-based cells: 400nm, 600nm, and 800nm. LSCF-GDC oxygen electrode with 600nm thickness is the one from previous chapter investigated. Figure 5-4 shows the result and by thickness optimization, the cell performed extraordinarily at 500°C. 1.05 A/cm<sup>2</sup> was achieved at 0.5V, and 1.15 A/cm<sup>2</sup> was consumed by the cell at 1.3 V. This amount is even far more than the one that this study achieved with electrolyte optimization at chapter 4 (0.96 A/cm<sup>2</sup>). However, its low OCV (0.82V) remains as an assignment to be further dealt with.

## 5.4. Conclusion

This chapter focused on developing thin film LSCF-GDC

oxygen electrode for thin film RSOC. Fabrication of the electrode was done by co-sputtering process. Optimum composition of LSCF-GDC was investigated by electrochemically testing on electrolyte-supported cells. After then, selected composition of LSCF-GDC was applied on AAO-based cells and further optimized. As a result, it was turned out that 400nm of <100-80> combination suits the best on AAO-based cell. The final cell achieved 1.15 A/cm<sup>2</sup> at 1.3V, which is by far the best performance over any reported literatures.

## 6. Concluding Remarks

This thesis developed thin-film solid oxide cells for reversible operation at low temperature (500°C) using the co-sputtering method. AAO support, Ni-YSZ steam electrode, YSZ electrolyte, and LSCF-GDC oxygen electrode were fabricated and optimized, especially on their microstructures. For the AAO support, three types of the average pore diameter were examined for pursuing suitability as support of thin film RSOC. AAO template with the largest pore size (250nm) showed the best suitability for the support of RSOC, primarily due to the smooth access of steam and

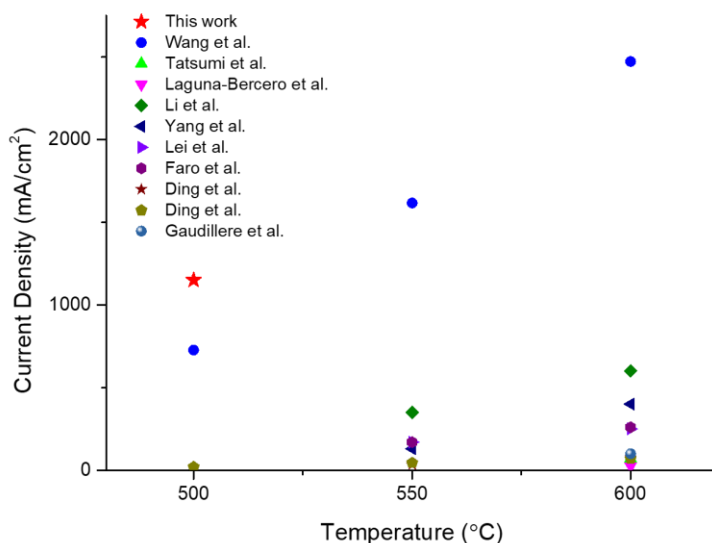


Figure 6-1. Literature data on electrolysis current at 1.3V by different operating temperature.

emission of products. The Ni-YSZ steam electrode was optimized to have 800 nm, deposited by 200W of DC power on Ni and 25W of RF power on Y/Zr.

The YSZ electrolyte was optimized by controlling target substrate distance and substrate rotation speed. It turned out that these variations in the physical configuration of the sputtering process impacted the YSZ thin film's crystallinity and interface properties. The distinguished film quality led to superior ohmic resistance and charge transfer impedance, allowing the RSOC to have much-improved reversibility.

Finally, the LSCF-GDC oxygen electrode was fabricated via the co-sputtering method. The primary aim of restructuring the oxygen electrode is to secure the linear path of evolved oxygen from the electrolyte-oxygen electrode interface. Therefore, the effort in chapter 5 was dedicated to fabricating the columnar electrode constitution. By securing the optimized LSCF-GDC composition and microstructure, the electrolysis current density at 1.3V and 500°C achieved 1.15 A/cm<sup>2</sup>, higher than any other literature reported so far.

Fabricating SOEC or RSOC using a thin film platform or using sputtering has never been reported in the literature so far.

Furthermore, the achievement this thesis has made exceeds any reported literature in terms of the electrolysis current density ( $1.15 \text{ A/cm}^2$ ) at  $1.3\text{V}$  and  $500^\circ\text{C}$ . According to the author's knowledge, this value is the highest current density among the reported values.

The result indicates that improved platform and microstructure of RSOC greatly enhance the performance even with the conventional materials. A more dramatic increase of performance can be made if newly developed materials, such as proton-conducting electrolytes, are used with the thin film platforms. As the sputtering process has been widely used commercially, such as in semiconductor fields, adopting the sputtering process for fabrication of RSOC steps forward to the propagation of RSOC in real life.

## Bibliography

- [1] J. Smith, S.Korea to raise emissions reduction goal to 40% by 2030, Reuters, <https://www.reuters.com/world/asia-pacific/skorea-raise-emissions-reduction-goal-40-by-2030-2021-10-08/>, Oct 8, 2021 (accessed October 25, 2021)
- [2] C. Stockwell, A. Geiges, D. Ramalope, M. Gidden, B. Hare, H. Fekete, S. Gonzales-Zuñiga, F. Hans, N. Höhne, C. Baxter, D. Arslan, M. Beer, Warming Projections Global Update, Climate Action Tracker, May 2021
- [3] P.-E. Franc, At the heart of the energy transition, Air Liquide, March 2020
- [4] H.-Y. Jung, S. Park, BN. Popov, Journal of Power Sources, 191 (2009) 357–361.
- [5] S.S. Dhrab, K. Sopian, M.A. Alghoul, M.Y. Sulaiman, Renewable and Sustainable Energy Reviews, 13 (2009) 1663–1668.
- [6] J. Pettersson, B. Ramsey, D. Harrison, Journal of Power Sources, 157 (2006) 28–34.
- [7] R. O'Hayre, S.-W. Cha, W. Colella, F.B. Prinz, Fuel Cell Fundamentals, John Wiley & Sons, Inc, Hoboken, NJ, USA, 2016.
- [8] M.B. Mogensen, Current Opinion in Electrochemistry, 21 (2020) 265–273.

- [9] S.Y. Gómez, D. Hotza, *Renewable and Sustainable Energy Reviews*, 61 (2016) 155–174.
- [10] Q. Fu, C. Mabilat, M. Zahid, A. Brisse, L. Gautier, *Energy & Environmental Science*, 3 (2010).
- [11] A. Hauch, R. Kungas, P. Blennow, A.B. Hansen, J.B. Hansen, B.V. Mathiesen, M.B. Mogensen, *Science*, 370 (2020).
- [12] Y. Zheng, J. Wang, B. Yu, W. Zhang, J. Chen, J. Qiao, J. Zhang, *Chem Soc Rev*, 46 (2017) 1427–1463.
- [13] Y. Wang, W. Li, L. Ma, W. Li, X. Liu, *Journal of Materials Science & Technology*, 55 (2020) 35–55.
- [14] K.F. Chen, S.P. Jiang, *International Journal of Hydrogen Energy*, 36 (2011) 10541–10549.
- [15] M. Keane, M.K. Mahapatra, A. Verma, P. Singh, *International Journal of Hydrogen Energy*, 37 (2012) 16776–16785.
- [16] M. Chen, in, *ETH Zurich*, 2005.
- [17] J. Laurencin, M. Hubert, D.F. Sanchez, S. Pylypko, M. Morales, A. Morata, B. Morel, D. Montinaro, F. Lefebvre–Joud, E. Siebert, *Electrochimica Acta*, 241 (2017) 459–476.
- [18] Z. Pan, Q. Liu, M. Ni, R. Lyu, P. Li, S.H. Chan, *International Journal of Hydrogen Energy*, 43 (2018) 5437–5450.
- [19] T. Wu, W. Zhang, Y. Li, Y. Zheng, B. Yu, J. Chen, X. Sun,

Advanced Energy Materials, 8 (2018).

[20] R. Knibbe, M.L. Traulsen, A. Hauch, S.D. Ebbesen, M. Mogensen, *Journal of The Electrochemical Society*, 157 (2010).

[21] M.A. Laguna-Bercero, R. Campana, A. Larrea, J.A. Kilner, V.M. Orera, *Journal of Power Sources*, 196 (2011) 8942–8947.

[22] K. Chen, S.P. Jiang, *Journal of The Electrochemical Society*, 163 (2016) F3070–F3083.

[23] D. The, S. Grieshammer, M. Schroeder, M. Martin, M. Al Daroukh, F. Tietz, J. Schefold, A. Brisse, *Journal of Power Sources*, 275 (2015) 901–911.

[24] Z. Jiao, N. Takagi, N. Shikazono, N. Kasagi, *Journal of Power Sources*, 196 (2011) 1019–1029.

[25] A. Gubner, E.C.S. Proceedings Volumes, 1997–40 (1997) 844–850.

[26] Y.H. Lee, I. Chang, G.Y. Cho, J. Park, W. Yu, W.H. Tanveer, S.W. Cha, *International Journal of Precision Engineering and Manufacturing–Green Technology*, 5 (2018) 441–453.

[27] A. Evans, A. Bieberle-Hutter, J.L.M. Rupp, L.J. Gauckler, *Journal of Power Sources*, 194 (2009) 119–129.

[28] J.H. Shim, C.-C. Chao, H. Huang, F.B. Prinz, *Chem Mater*, 19 (2007) 3850–3854.

[29] J. An, Y.B. Kim, J. Park, T.M. Gur, F.B. Prinz, *Nano Lett*, 13 (2013) 4551–4555.

[30] Y.H. Lee, H. Ren, E.A. Wu, E.E. Fullerton, Y.S. Meng, N.Q. Minh, *Nano Lett*, 20 (2020) 2943–2949.

[31] W. Yu, in: Department of Mechanical and Aerospace Engineering, Seoul National University, Seoul, 2020.

[32] M. Zunic, L. Chevallier, F. Deganello, A. D’Epifanio, S. Licoccia, E. Di Bartolomeo, E. Traversa, *Journal of Power Sources*, 190 (2009) 417–422.

[33] P.J. Kelly, R.D. Arnell, *Vacuum*, 56 (2000) 159–172.

[34] S. Hong, Y. Lim, H. Yang, J. Bae, Y.-B. Kim, *Journal of Materials Chemistry A*, 5 (2017) 2029–2036.

[35] I. Chang, P. Heo, S.W. Cha, *Thin Solid Films*, 534 (2013) 286–290.

[36] F.J. Garcia–Garcia, F. Yubero, A.R. González–Elipe, S.P. Balomenou, D. Tsiplakides, I. Petrakopoulou, R.M. Lambert, *International Journal of Hydrogen Energy*, 40 (2015) 7382–7387.

[37] Y. Lim, H. Lee, S. Hong, Y.-B. Kim, *Journal of Power Sources*, 412 (2019) 160–169.

[38] T. Tsai, S.A. Barnett, *Journal of Vacuum Science & Technology A*, 13 (1995) 1073–1077.

- [39] A.F. Jankowski, J.P. Hayes, *Surface and Coatings Technology*, 76–77 (1995) 126–131.
- [40] O. Yamamoto, Y. Takeda, R. Kanno, M. Noda, *Solid State Ionics*, 22 (1987) 241–246.
- [41] W. Lee, S.J. Park, *Chem Rev*, 114 (2014) 7487–7556.
- [42] W. Yu, Y. Lim, S. Lee, A. Pandiyan, G.Y. Cho, S.W. Cha, *Journal of Materials Chemistry A*, 8 (2020) 21668–21679.
- [43] H. Ren, Y.H. Lee, E.A. Wu, H. Chung, Y.S. Meng, E.E. Fullerton, N.Q. Minh, *A.C.S. Applied Energy Materials*, 3 (2020) 8135–8142.
- [44] I. Chang, S. Ji, J. Park, M.H. Lee, S.W. Cha, *Advanced Energy Materials*, 5 (2015).
- [45] M.S. Lee, S. Lee, W. Jeong, S. Ryu, W. Yu, Y.H. Lee, G.Y. Cho, S.W. Cha, *International Journal of Hydrogen Energy*, 46 (2021) 36445–36453.
- [46] M.S. Lee, in: *Department of Mechanical Engineering, Seoul National University, Seoul, 2020.*
- [47] S. Ha, P.-C. Su, S.-W. Cha, *Journal of Materials Chemistry A*, 1 (2013).
- [48] T. Setoguchi, K. Okamoto, K. Eguchi, H. Arai, *Journal of The Electrochemical Society*, 139 (1992) 2875–2880.
- [49] Y. Liu, Z. Shao, T. Mori, S.P. Jiang, *Materials Reports: Energy*,

1 (2021).

[50] I.V. Ionov, N.S. Sochugov, A.A. Soloviev, A.N. Kovalchuk, A.O. Tcybenko, T.I. Sigfusson, in: 2012 7th International Forum on Strategic Technology (IFOST), IEEE, Tomsk, Russia, 2012.

[51] JR Kong, KN Sun, D.R. Zhou, N.Q. Zhang, J. Mu, J.S. Qiao, *Journal of Power Sources*, 166 (2007) 337–342.

[52] I. Kagomiya, S. Kaneko, K. Kakimoto, K. Park, K.H. Cho, *Fuel Cells*, 15 (2015) 90–97.

[53] E. Rezugina, A.L. Thomann, H. Hidalgo, P. Brault, V. Dolique, Y. Tessier, *Surf Coat Tech*, 204 (2010) 2376–2380.

[54] H.J. Kim, M.J. Kil, J. Lee, B.C. Yang, D. Go, Y. Lim, Y.B. Kim, J. An, *Applied Surface Science*, 538 (2021).

[55] M.B. Mogensen, M. Chen, H.L. Frandsen, C. Graves, J.B. Hansen, K.V. Hansen, A. Hauch, T. Jacobsen, S.H. Jensen, T.L. Skaftø, X. Sun, *Clean Energy*, 3 (2019) 175–201.

[56] J. Park, Y. Lee, I. Chang, W. Lee, S.W. Cha, *Thin Solid Films*, 584 (2015) 125–129.

[57] A. Sciazko, T. Shimura, Y. Komatsu, N. Shikazono, *Journal of Thermal Science and Technology*, 16 (2021) JTST0013–JTST0013.

[58] P. Moçoteguy, A. Brisse, *International Journal of Hydrogen Energy*, 38 (2013) 15887–15902.

- [59] NQ. Minh, *Journal of the American Ceramic Society*, 76 (1993) 563–588.
- [60] S. Lee, Y. Lee, J. Park, W. Yu, G.Y. Cho, Y. Kim, S.W. Cha, *Renewable Energy*, 144 (2019) 123–128.
- [61] J.Y. Paek, I. Chang, J.H. Park, S. Ji, S.W. Cha, *Renewable Energy*, 65 (2014) 202–206.
- [62] S. Ryu, W. Yu, I. Chang, T. Park, G.Y. Cho, S.W. Cha, *Ceramics International*, 46 (2020) 12648–12655.
- [63] D.J. Brett, A. Atkinson, N.P. Brandon, S.J. Skinner, *Chem Soc Rev*, 37 (2008) 1568–1578.
- [64] JTS. Irvine, D. Neagu, M.C. Verbraeken, C. Chatzichristodoulou, C. Graves, M.B. Mogensen, *Nature Energy*, 1 (2016).
- [65] M.S. Khan, X. Xu, R. Knibbe, Z. Zhu, *Renewable and Sustainable Energy Reviews*, 143 (2021).

## 국 문 초 록

글로벌 기후위기가 목전에 직면하면서 탈탄소화에 대한 요구가 가파르게 증가하고 있다. 그에 대한 해답으로 수소경제 전환이 주목받고 있으나, 진정한 수소경제를 달성하기 위한 그린수소 생산은 수소연료 사용과는 다른 측면에서 발목을 잡고 있다. 높은 생산비용이 그린수소 도입을 막고 있어, 수전해 과정에 필요한 전기 및 열에너지 절감을 통한 수소생산비용 감소가 절실하다. 따라서 수전해전지의 고효율화를 통한 필요 전기에너지량 감소 및 작동온도 감소가 필수적이다.

고체산화물전지를 박막 플랫폼을 기반으로 제작하면 전극의 주상구조를 통한 반응물/생성물의 원활한 공급과 배출 및 반응영역 확대를 통한 활발한 반응 동역학을 기반으로 이러한 문제를 해결할 수 있다. 따라서, 본 연구에서는 스퍼터링 공정을 이용해 박막 고체산화물전지를 개발하고 저온( $<500^{\circ}\text{C}$ )에서의 가역작동을 검증했다. 마그네트론 스퍼터링 공정을 사용해 양극산화 알루미늄 기판(AAO) 기반의 박막 고체산화물전지를 제작했으며, Ni-YSZ/YSZ/LSCF-GDC의 연료극/전해질/공기극 구조를 구현했다. 각 요소별 스퍼터링 공정변수 최적화를 통해 마이크로구조 최적화를 진행했다. 결과적으로  $500^{\circ}\text{C}$ 의 작동온도와 열중립전압(1.3V)에서 지금까지 보고된 어떤 문헌의 값보다 높은 전해 전류밀도를 달성했다.

연료극인 Ni-YSZ는 각 물질의 조성비, 전극 두께, 미세구조 등을 스퍼터링 공정 변수 최적화를 통해 향상된 가역성을 갖도록 성능 최적화를 진행했다. 이에 따라 전해조 작동시 전류가 230% 이상 향상되는 효과를 달성했다. YSZ 전해질 제작에서는 스퍼터링 시스템의 타겟-기판 거리(TSD), 기판회전 속도(SRS)를 조절해 전해질의 성능과 전해질/공기극 계면특성 향상을 꾀했다. 결과적으로 YSZ 전해질의 결정성과 전해질 표면 미세구조의 개선으로 인해 수전해 성능이 대폭 향상된 것을 확인했다. 공기극은 LSCF-GDC 물질을 코-스퍼터링 공정을 통해 제작했다. LSCF와 GDC의 물질 조성, 전극 두께 등을 최적화하여 최고성능을 발휘하는 제작공정을 기반으로 전극 제작이 이뤄졌다.

본 연구를 통해 세계 최초로 스퍼터링 공정을 이용한 가역작동 박막 고체산화물전지를 제작해 실증했다. 이를 이용해 450°C 및 500°C의 작동온도와 열중립전압(1.3V)에서 그간 보고된 어떤 전해 전류밀도보다 높은 세계 최고성능 또한 달성했다. 박막화를 통한 전극-전해질 계면특성 향상을 통해 반응 동역학을 획기적으로 개선함으로써 저온에서 고성능의 고체산화물전지 가역작동을 실현할 수 있었다. 이로써 박막 플랫폼을 기반으로 한 고체산화물전지는 저온 가역작동에서 잠재력이 큰 우수한 플랫폼으로 기능할 수 있다는 것이 본 연구를 통해 입증됐다.